

Boundary control in computational haemodynamics

Journal Article**Author(s):**

Koltukluoglu, Taha S.; Blanco, Pablo J.

Publication date:

2018-07-25

Permanent link:

<https://doi.org/10.3929/ethz-b-000278019>

Rights / license:

[In Copyright - Non-Commercial Use Permitted](#)

Originally published in:

Journal of Fluid Mechanics 847, <https://doi.org/10.1017/jfm.2018.329>

Boundary control in computational haemodynamics

Taha S. Koltukluoğlu^{1,†} and Pablo J. Blanco²

¹Seminar for Applied Mathematics, Swiss Federal Institute of Technology (ETH), 8092 Zürich, Switzerland

²National Laboratory for Scientific Computing, (LNCC/MCTIC), 25651-075 Petrópolis, Brazil

(Received 10 August 2017; revised 13 February 2018; accepted 14 April 2018;
first published online 21 May 2018)

In this work, a data assimilation method is proposed following an optimise-then-discretise approach, and is applied in the context of computational haemodynamics. The methodology aims to make use of phase-contrast magnetic resonance imaging to perform optimal flow control in computational fluid dynamic simulations. Flow matching between observations and model predictions is performed in luminal regions, excluding near-wall areas, improving the near-wall flow reconstruction to enhance the estimation of related quantities such as wall shear stresses. The proposed approach remarkably improves the flow field at the aortic root and reveals a great potential for predicting clinically relevant haemodynamic phenomenology. This work presents model validation against an analytical solution using the standard 3-D Hagen–Poiseuille flow, and validation with real data involving the flow control problem in a glass replica of a human aorta imaged with a 3T magnetic resonance scanner. *In vitro* experiments consist of both a numerically generated reference flow solution, which is considered as the ground truth, as well as real flow MRI data obtained from phase-contrast flow acquisitions. The validation against the *in vitro* flow MRI experiments is performed for different flow regimes and model parameters including different mesh refinements.

Key words: blood flow, control theory, variational methods

1. Introduction

Wall shear stresses (WSSs) in arterial vessels have long been hypothesised to play a major role in the onset and progress of endothelial disorders. The dependence of endothelial cell function under different flow conditions and the impact of WSSs in the development of atherosclerosis have been described in earlier studies (Texon, Imparato & Helpert 1965; Ku *et al.* 1985; Zarins *et al.* 1987; Zand *et al.* 1991; Walpole, Gotlieb & Langille 1993; Malek, Alper & Izumo 1999). A brief review of the underlying hypotheses for haemodynamic theories of atherogenesis was given by Gessner (1973). More recent studies have explored the processes at the molecular, cellular and vascular levels, and supported the role of low WSSs in the generation

† Email addresses for correspondence: ktaha@ethz.ch, koltukluoglu@gmail.com

of coronary atherosclerosis and vascular remodelling (Chatzizisis *et al.* 2007; Chiu & Chien 2011). The effects of haemodynamic forces were discussed by Yoshida *et al.* (1990), considering the differences in the biological fine structures of arterial walls in the human aorta and the endothelial morphology at bifurcations in rabbit aorta. Moreover, characterisation of blood flow near the aortic wall plays an important role in the diagnosis of aortic aneurysms and their risk of rupture (Vorp *et al.* 1996; Vorp & Geest 2005).

Thus, the evaluation of shear stresses over the arterial wall, using different computational strategies to either simulate or reconstruct blood flow, has gained increasing interest in the cardiovascular research field. A basic approach to this problem consists of using data extracted from medical images to construct patient-specific vascular models and to perform computational fluid dynamic (CFD) simulations of blood flow in these geometric models. The major drawback in such approaches lies in the lack of data to correctly set up boundary conditions (BCs) for the isolated arterial districts of interest. Rapidly, the patient-specificity is lost when using generic criteria to prescribe such BCs in CFD simulations.

A further step resides in using more advanced image acquisition techniques in an attempt to retrieve flow field measurements and merge them into the CFD simulations, thus providing more accurate patient-specific predictions. In this context, different methods exist to reconstruct the velocity field in a certain region of interest. Several works have already been reported that address this problem using particle image velocimetry (PIV), ultrasound and 4-D phase-contrast magnetic resonance imaging (4-D flow MRI). A comprehensive review of several methods for flow reconstruction and the assessment of WSSs is presented by Katritsis *et al.* (2007).

The use of PIV is known to be limited to *in vitro* studies and cannot be applied to the study of blood flow in *in vivo* conditions (Hochareon *et al.* 2004). On the other hand, ultrasound imaging allows the extraction of 2-D information, thus requiring a 3-D flow reconstruction process, which is prone to lacking accuracy in view of the incomplete nature of the data. Another limitation of ultrasound is that the WSSs can only be estimated with acceptable accuracy in relatively straight arteries (Reneman, Arts & Hoeks 2006). In turn, 4-D flow MRI offers the advantage of three-directional blood flow quantification with three-dimensional spatial encoding. Image reconstruction from the MRI data acquisition yields 3-D CINE magnitude images (anatomical data) and three phase difference images (velocity data), corresponding to the components of the 3-D velocity field. Moreover, MRI can be used in *in vivo* scenarios non-invasively. Recent advances in MRI have revealed great diagnostic potential in haemodynamics applications (Markl *et al.* 2012; Kolipaka *et al.* 2016). Nevertheless, 4-D flow MRI also suffers from important limitations for the accurate quantification of blood flow in regions close to the arterial walls (near-wall regions), which is of the utmost importance for patient-specific estimation of the WSS field. Due to the limited image resolution, the acquired signals within the voxels at boundaries are obtained partially by the moving spins in the flowing blood and partially by the steady behaviour of the arterial tissue. This artefact is known as the partial volume effect (Thang, Blatter & Parker 1995; Shaaban & Duerinckx 2000; Bouillot *et al.* 2018).

Correct definition of the flow problem requires knowledge of the initial conditions and BCs, as well as the flow properties, i.e. blood density and blood viscosity. However, due to the limitations of the aforementioned imaging techniques, in particular the BCs are usually not available or cannot be measured accurately. Especially, the problem of a correct assessment of the BCs for such defective data

has been the point of attention for a long time. Several studies have been reported on the effects of idealised versus measured inflow BCs for patient-specific simulations of carotid bifurcation or human aorta (Campbell *et al.* 2012; Morbiducci *et al.* 2013). Additionally, a sensitivity analysis with respect to different BCs was reported by Cito, Pallarés & Vernet (2014). Furthermore, a recent report provided by Pirola *et al.* (2017) discussed the importance of the choice of BCs on the final results.

As a result of the aforementioned advantages and limitations of current imaging technologies, 4-D flow MRI procedures have become increasingly frequent in routine towards the improvement of patient-specific CFD simulations. Classical CFD methods (supported by MRI) usually apply fixed BCs at the inlet of the arterial domain based on the noisy measurements extracted from the 4-D flow MRI data (Hardman *et al.* 2013; Pirola *et al.* 2017). This is why recent studies have concentrated on optimal control strategies to alter BCs in such a way that the flow in the lumen matches the observations according to certain criteria. Optimal control supported by observations has been referred to as data assimilation (DA). Such studies were first and mainly applied in meteorology, physical oceanography and atmospheric flows (Council 1991; Ide *et al.* 1997). Due to the shortcomings in the classical CFD approach (CFD employing noisy data as BCs), DA has achieved elevated attention in the cardiovascular research field over the last decade.

Data assimilation procedures in haemodynamics were anticipated a decade ago for the prescription of flow rates in rigid and compliant domains (Formaggia, Veneziani & Vergara 2008, 2010). Additional preliminary results of DA in tubular structures were reported by D'Elia & Veneziani (2010*a*) based on 2-D Stokes flow simulations. The convergence rate and noise sensitivity were investigated based on artificially generated noisy data. In D'Elia & Veneziani (2010*b*), their work was extended to the Oseen problem. This strategy was employed in combination with a fixed point method to solve the Navier–Stokes equations and to perform flow matching in synthetically generated datasets using different mesh refinements. In a further study, these authors extended their tests to an axis-symmetric cylinder and a 2-D geometry resembling a carotid artery (D'Elia, Perego & Veneziani 2012*b*). These studies were based on a discretise-then-optimize (DO) approach, where the equations are first discretised and the optimisation is performed thereafter. Numerical results were mostly based on 2-D simplified geometries or on problems with rotational symmetry. These works were some of the first attempts to perform DA in blood flow simulations. However, real flow MRI measurements were not available in these studies.

In a recent work, DA was performed using more realistic vascular geometries (Tiago, Guerra & Sequeira 2016). First, a comparison between Dirichlet and Neumann boundary control was reported, with the validation based on an idealised 2-D geometry with known solution. Second, numerical results were presented using a realistic 3-D geometry of a saccular brain aneurysm. The application of velocity control (Dirichlet BC) was claimed to recover the flow field better than the application of pressure control (Neumann BC). However, the flow data were synthetic and experiments with real 4-D flow MRI measurements were not available. Furthermore, they also applied the DO approach as a solution strategy. In Collis & Heinkenschloss (2002), however, the authors concluded that the optimise-then-discretise (OD) approach (where the mathematical optimisation is first performed at the continuum level and the resulting set of equations are then discretised thereafter) has better asymptotic convergence properties and leads to better adjoint approximations.

In this work, we propose a data assimilation method for 3-D steady-state blood flow simulations following the OD approach. To the best of the authors' knowledge,

this is the first work to perform OD-based 3-D optimal flow control in the field of computational haemodynamics using true data acquisitions from 4-D flow MRI. The optimisation procedure is driven by the gradient of a given cost functional, computed within a variational framework. A Lagrangian method is employed for the calculation of the sensitivities from which the adjoint problem is derived. Further, the proposed approach considers cost functionals in the flow-matching formulation including the inlet and outlet boundaries (in addition to flow matching in the volume of the domain). While previous studies mostly count on validations with known numerical solutions in simplified 2-D geometries, in this work we perform 3-D validation studies relying on both an analytical solution based on the Hagen–Poiseuille flow and a numerical solution generated using the physical phantom aorta. We also present a sensitivity analysis with respect to changes in the optimisation parameters. Considering the noisy nature of 4-D flow MRI measurements, a universal outlier detection scheme is applied prior to the mapping of the flow field in the computational domain. Besides, a divergence-free space projection is employed to recover back the solenoidal property of the measured flow field. An additional sensitivity analysis with respect to changes in the flow-matching domain is developed, which is important in determining the region of interest for the DA procedure. The optimisation solver was tested for different initial flow guesses, demonstrating the sensitivity in the numerical results. Finally, the boundary flow control formulation and the preprocessing pipeline are combined to reconstruct the flow field in near-wall regions in a glass replica of the human aorta. For the latter, the methodology was tested for different flow regimes characterised by Reynolds numbers (Re) up to 2100, and mesh analysis was performed with different numbers of cells. The proposed strategy remarkably improves the flow field at the aortic root and reveals a great potential for predicting clinically relevant haemodynamic phenomenology.

2. Mathematical formulation

2.1. Optimisation problem

Let us define a bounded Lipschitz domain $\Omega \subset \mathbb{R}^3$ along with its boundary $\partial\Omega = \Gamma_i \cup \Gamma_o \cup \Gamma_w$, where $\Gamma_i, \Gamma_o, \Gamma_w \subset \mathbb{R}^3$ stand for the inlet, outlet and arterial wall boundaries respectively. Figure 1(a) illustrates such a domain resembling an aortic vascular geometry (to be used later in §5). We further define a contracted subdomain $\Omega_s \subset \Omega$ with boundary $\partial\Omega_s = \Gamma_{si} \cup \Gamma_{so} \cup \Gamma_{sw}$, where $\Gamma_{si} \subset \Gamma_i$ and $\Gamma_{so} \subset \Gamma_o$ (see figure 1b). The incompressible steady flow of a Newtonian fluid is considered in Ω . The inflow at Γ_i is prescribed by the function $\mathbf{g} = \mathbf{g}(\mathbf{x}) : \Gamma_i \rightarrow \mathbb{R}^3$, whereas the density and dynamic viscosity of the fluid are represented by ρ and μ respectively. At the outflow, Γ_o , a traction-free boundary (i.e. a homogeneous Neumann BC) is considered. This hypothesis is exact when the flow is fully developed, and it is physiologically reasonable in the present context. We highlight the fact that the function \mathbf{g} is such that $\mathbf{g}|_{\gamma_i} = \mathbf{0}$, where γ_i is the boundary of surface Γ_i . In what follows, $L^2(\Omega)$ stands for the space of square integrable scalar functions in Ω , while $\mathbf{H}^1(\Omega)$ is the space of square integrable vector functions whose first derivatives are also square integrable functions in Ω . The blood flow velocity, $\mathbf{u} \in \mathcal{U}^*$, with

$$\mathcal{U}^* = \{\mathbf{v} \in \mathbf{H}^1(\Omega) \mid \operatorname{div} \mathbf{v} = 0, \mathbf{v}|_{\Gamma_w} = \mathbf{0}, \mathbf{v}|_{\Gamma_i} = \mathbf{g}\}, \quad (2.1)$$

is a solution of the steady-state Navier–Stokes equations, which are written in variational form as follows:

$$\text{find } \mathbf{u} \in \mathcal{U}^* \text{ such that } \int_{\Omega} [\rho(\nabla \mathbf{u})\mathbf{u} \cdot \hat{\mathbf{u}} + 2\mu \nabla^s \mathbf{u} \cdot \nabla^s \hat{\mathbf{u}}] d\Omega = 0, \quad \forall \hat{\mathbf{u}} \in \hat{\mathcal{U}}^*, \quad (2.2)$$

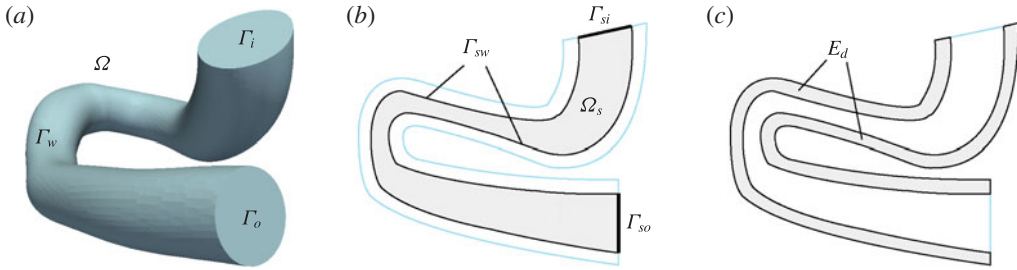


FIGURE 1. (Colour online) The computational domain. (a) The domain Ω along with boundaries Γ_i , inlet, Γ_o , outlet, and Γ_w , wall. (b) The flow-matching domain $\Omega_s \subset \Omega$ with boundaries $\partial\Omega_s = \Gamma_{si} \cup \Gamma_{so} \cup \Gamma_{sw}$, which is at a distance s (mm) from Γ_w . (c) The error measurement domain E_d , which is within d (mm) distance of Γ_w .

where the strain rate tensor is defined as $\nabla^s(\cdot) = [\nabla(\cdot) + (\nabla(\cdot))^T]/2$ and

$$\widehat{\mathcal{U}}^* = \{\hat{\mathbf{v}} \in \mathbf{H}^1(\Omega) \mid \text{div } \hat{\mathbf{v}} = 0, \hat{\mathbf{v}}|_{\Gamma_w} = \mathbf{0}, \hat{\mathbf{v}}|_{\Gamma_i} = \mathbf{0}\}. \tag{2.3}$$

The constraints $\text{div } \mathbf{u} = 0$ and $\mathbf{u}|_{\Gamma_i} = \mathbf{g}$ can be relaxed using the corresponding Lagrange multipliers p and \mathbf{r} . Further, we introduce the space $\mathcal{U} = \{\mathbf{v} \in \mathbf{H}^1(\Omega) \mid \mathbf{v}|_{\Gamma_w} = \mathbf{0}\}$ and the space $\mathbf{H}^{-1/2}(\Gamma_i)$, which is the dual space of $\mathbf{H}^{1/2}(\Gamma_i)$ (in the sense given by the pairing $\langle \mathbf{r}, \mathbf{u} \rangle_{\mathbf{H}^{-1/2}(\Gamma_i) \times \mathbf{H}^{1/2}(\Gamma_i)} = \int_{\Gamma_i} \mathbf{r} \cdot \mathbf{u} \, d\Gamma$). The problem (2.2) now becomes

$$\begin{aligned} \mathcal{P}_\Omega : \text{find } (\mathbf{u}, p, \mathbf{r}) \in \mathcal{U} \times L^2(\Omega) \times \mathbf{H}^{-1/2}(\Gamma_i) \text{ such that} \\ \int_\Omega [\rho(\nabla \mathbf{u}) \mathbf{u} \cdot \hat{\mathbf{u}} + 2\mu \nabla^s \mathbf{u} \cdot \nabla^s \hat{\mathbf{u}} - p \text{div } \hat{\mathbf{u}} - \hat{p} \text{div } \mathbf{u}] \, d\Omega \\ = \int_{\Gamma_i} \hat{\mathbf{r}} \cdot (\mathbf{u} - \mathbf{g}) \, d\Gamma + \int_{\Gamma_i} (\mathbf{r} \cdot \hat{\mathbf{u}}) \, d\Gamma, \quad \forall (\hat{\mathbf{u}}, \hat{p}, \hat{\mathbf{r}}) \in \mathcal{U} \times L^2(\Omega) \times \mathbf{H}^{-1/2}(\Gamma_i). \end{aligned} \tag{2.4}$$

For the control flow problem, we assume that some observations $\tilde{\mathbf{u}}^t \in \Omega$ are available. We want to find a velocity field \mathbf{u} such that it better matches the observations and, at the same time, is constrained to be a solution of problem \mathcal{P}_Ω . In what follows, ∇_τ denotes the surface gradient, whereas β and β_1 are arbitrary parameters for a Tikhonov regularisation and α is a positive real number. The parameters α , β and β_1 will often be denoted as optimisation parameters. Based on a user-defined cost function, \mathcal{O} , the aforementioned flow-matching problem can be cast as a mathematical optimisation problem, which reads as

$$\begin{aligned} \mathcal{P}_M : \text{find } \mathbf{g} \text{ that minimises } \mathcal{O}(\mathbf{g}) = \mathcal{O}^*(\mathbf{u}(\mathbf{g}), \mathbf{g}, \tilde{\mathbf{u}}^t) \text{ such that } \mathcal{P}_\Omega \text{ holds, where} \\ \mathcal{O}(\mathbf{g}) = \frac{\alpha}{2} \left(\int_{\Omega_s} |\mathbf{u}(\mathbf{g}) - \tilde{\mathbf{u}}^t|^2 \, d\Omega + \int_{\Gamma_{si}} |\mathbf{u}(\mathbf{g}) - \tilde{\mathbf{u}}^t|^2 \, d\Gamma + \int_{\Gamma_{so}} |\mathbf{u}(\mathbf{g}) - \tilde{\mathbf{u}}^t|^2 \, d\Gamma \right) \\ + \frac{\beta}{2} \int_{\Gamma_i} |\mathbf{g}|^2 \, d\Gamma + \frac{\beta_1}{2} \int_{\Gamma_i} |\nabla_\tau \mathbf{g}|^2 \, d\Gamma. \end{aligned} \tag{2.5}$$

The flow-matching metric is defined on Ω_s , Γ_{si} and Γ_{so} , which are considered as the trust region of experimental observations (see figure 1b). The well-posedness of the problem \mathcal{P}_M has been addressed by Guerra, Sequeira & Tiago (2015).

The user-defined cost function contains two types of terms, those to enforce the matching between the model prediction and the available observations, and those to deliver a regularised mathematical problem. Concerning (2.5), the first three terms are responsible for the flow matching, while the latter two terms provide a penalisation for the control function not to grow unboundedly, and, at the same time, to force a certain regularity over the control. The choices of these terms were also motivated by Gunzburger & Manservigi (2000).

2.2. Optimality conditions

To obtain the necessary optimality conditions for the optimisation problem \mathcal{P}_M , and to avoid the calculation of the derivative of the velocity field with respect to the function \mathbf{g} , it is convenient to recast the problem of constrained optimisation as a saddle point problem. Correspondingly, we then construct the Lagrangian functional to relax the dependence of \mathbf{u} on \mathbf{g} as follows:

$$\begin{aligned} \mathcal{L}(\mathbf{g}, \mathbf{u}, p, \mathbf{r}, \lambda_u, \lambda_p, \lambda_r) &= \mathcal{O}^*(\mathbf{u}, \mathbf{g}, \tilde{\mathbf{u}}^t) - \int_{\Gamma_i} \lambda_r \cdot (\mathbf{u} - \mathbf{g}) \, d\Gamma - \int_{\Gamma_i} \mathbf{r} \cdot \lambda_u \, d\Gamma \\ &+ \int_{\Omega} [\rho(\nabla \mathbf{u})\mathbf{u} \cdot \lambda_u + 2\mu \nabla^s \mathbf{u} \cdot \nabla^s \lambda_u - p \operatorname{div} \lambda_u - \lambda_p \operatorname{div} \mathbf{u}] \, d\Omega, \end{aligned} \tag{2.6}$$

with $(\mathbf{g}, \mathbf{u}, p, \mathbf{r}, \lambda_u, \lambda_p, \lambda_r) \in \mathbf{H}_{00}^{1/2}(\Gamma_i) \times \mathcal{U} \times L^2(\Omega) \times \mathbf{H}^{-1/2}(\Gamma_i) \times \mathcal{U} \times L^2(\Omega) \times \mathbf{H}^{-1/2}(\Gamma_i)$, where $\mathbf{H}_{00}^{1/2}(\Gamma_i)$ is the space of traces over Γ_i of $\mathbf{H}^1(\Omega)$ functions that are zero over γ_i , the boundary of surface Γ_i . Further, let us consider the perturbations $(\hat{\cdot})$ to the fields (\cdot) above as $(\cdot) + \tau(\hat{\cdot})$ (where τ is a real number that aids in the calculation of the Gâteaux derivative but that is ultimately immaterial for the result), that is,

$$\mathbf{g} \rightarrow \mathbf{g} + \tau \hat{\mathbf{g}}, \quad \mathbf{g}, \hat{\mathbf{g}} \in \mathbf{H}_{00}^{1/2}(\Gamma_i), \tag{2.7}$$

$$\mathbf{u} \rightarrow \mathbf{u} + \tau \hat{\mathbf{u}}, \quad \mathbf{u}, \hat{\mathbf{u}} \in \mathcal{U}, \tag{2.8}$$

$$p \rightarrow p + \tau \hat{p}, \quad p, \hat{p} \in L^2(\Omega), \tag{2.9}$$

$$\mathbf{r} \rightarrow \mathbf{r} + \tau \hat{\mathbf{r}}, \quad \mathbf{r}, \hat{\mathbf{r}} \in \mathbf{H}^{-1/2}(\Gamma_i), \tag{2.10}$$

$$\lambda_u \rightarrow \lambda_u + \tau \hat{\lambda}_u, \quad \lambda_u, \hat{\lambda}_u \in \mathcal{U}, \tag{2.11}$$

$$\lambda_p \rightarrow \lambda_p + \tau \hat{\lambda}_p, \quad \lambda_p, \hat{\lambda}_p \in L^2(\Omega), \tag{2.12}$$

$$\lambda_r \rightarrow \lambda_r + \tau \hat{\lambda}_r, \quad \lambda_r, \hat{\lambda}_r \in \mathbf{H}^{-1/2}(\Gamma_i). \tag{2.13}$$

The Gâteaux derivative of the Lagrangian functional is denoted as follows:

$$\left\langle \frac{\partial \mathcal{L}}{\partial a}, \hat{a} \right\rangle = \left. \frac{d}{d\tau} \mathcal{L}(\dots, a + \tau \hat{a}, \dots) \right|_{\tau=0}. \tag{2.14}$$

Our goal is to compute the Gâteaux derivative of \mathcal{O} with respect to perturbation in \mathbf{g} ,

$$\left\langle \frac{\partial \mathcal{O}}{\partial \mathbf{g}}, \hat{\mathbf{g}} \right\rangle = \left. \frac{d}{d\tau} \mathcal{O}(\mathbf{g} + \tau \hat{\mathbf{g}}) \right|_{\tau=0}. \tag{2.15}$$

The critical points of the Lagrangian (2.6) contain information on the aforementioned Gâteaux derivative (2.15), and are characterised by

$$\left\langle \frac{\partial \mathcal{L}}{\partial (\lambda_u, \lambda_p, \lambda_r)}, \begin{pmatrix} \hat{\lambda}_u \\ \hat{\lambda}_p \\ \hat{\lambda}_r \end{pmatrix} \right\rangle = \mathbf{0}, \quad \left\langle \frac{\partial \mathcal{L}}{\partial (\mathbf{u}, p, \mathbf{r})}, \begin{pmatrix} \hat{\mathbf{u}} \\ \hat{p} \\ \hat{\mathbf{r}} \end{pmatrix} \right\rangle = \mathbf{0}, \quad \left\langle \frac{\partial \mathcal{L}}{\partial \mathbf{g}}, \hat{\mathbf{g}} \right\rangle = 0. \tag{2.16a-c}$$

Equations (2.16 a) and (2.16 b) describe the direct and the so-called adjoint equations to solve for the state variables $(\mathbf{u}, p, \mathbf{r})$ and the adjoint variables $(\lambda_u, \lambda_p, \lambda_r)$ respectively. Finally, (2.16 c) provides the optimality condition of the cost functional with respect to perturbations in \mathbf{g} . In particular, it also follows that

$$\left\langle \frac{\partial \mathcal{O}}{\partial \mathbf{g}}, \hat{\mathbf{g}} \right\rangle = \left\langle \frac{\partial \mathcal{L}}{\partial \mathbf{g}}, \hat{\mathbf{g}} \right\rangle \Bigg|_{\substack{(\mathbf{u}, p, \mathbf{r}) \text{ solution of direct problem} \\ (\lambda_u, \lambda_p, \lambda_r) \text{ solution of adjoint problem}}} . \tag{2.17}$$

Let us now compute the Gâteaux derivatives (2.16). We first obtain the direct problem by taking the derivative with respect to the variables $(\lambda_u, \lambda_p, \lambda_r)$. Then, the following problem is obtained:

$$\begin{aligned} \mathcal{P}_{sta}(\mathbf{g}): \text{ for } \mathbf{g} \in \mathbf{H}_{00}^{1/2}(\Gamma_i), \text{ determine } (\mathbf{u}, p, \mathbf{r}) \in \mathcal{U} \times L^2(\Omega) \times \mathbf{H}^{-1/2}(\Gamma_i) \text{ such that} \\ \left\langle \frac{\partial \mathcal{L}}{\partial \lambda_u}, \hat{\lambda}_u \right\rangle = \int_{\Omega} [\rho(\nabla \mathbf{u}) \mathbf{u} \cdot \hat{\lambda}_u + 2\mu \nabla^s \mathbf{u} \cdot \nabla^s \hat{\lambda}_u - p \operatorname{div} \hat{\lambda}_u] \, d\Omega \\ - \int_{\Gamma} \mathbf{r} \cdot \hat{\lambda}_u \, d\Gamma = 0, \quad \forall \hat{\lambda}_u \in \mathcal{U}, \end{aligned} \tag{2.18}$$

$$\left\langle \frac{\partial \mathcal{L}}{\partial \lambda_p}, \hat{\lambda}_p \right\rangle = - \int_{\Omega} \hat{\lambda}_p \operatorname{div} \mathbf{u} \, d\Omega = 0, \quad \forall \hat{\lambda}_p \in L^2(\Omega), \tag{2.19}$$

$$\left\langle \frac{\partial \mathcal{L}}{\partial \lambda_r}, \hat{\lambda}_r \right\rangle = - \int_{\Gamma} \hat{\lambda}_r \cdot (\mathbf{u} - \mathbf{g}) \, d\Gamma = 0, \quad \forall \hat{\lambda}_r \in \mathbf{H}^{-1/2}(\Gamma_i). \tag{2.20}$$

The Euler–Lagrange equations associated with (2.18)–(2.20) are the classical Navier–Stokes equations, which read as follows:

$$\rho(\nabla \mathbf{u}) \mathbf{u} - \mu \Delta \mathbf{u} + \nabla p = \mathbf{0} \quad \text{in } \Omega, \tag{2.21}$$

$$\operatorname{div} \mathbf{u} = 0 \quad \text{in } \Omega, \tag{2.22}$$

$$\mathbf{u} = \mathbf{0} \quad \text{on } \Gamma_w, \tag{2.23}$$

$$\mathbf{u} = \mathbf{g} \quad \text{on } \Gamma_i, \tag{2.24}$$

$$(-p\mathbf{I} + 2\mu \nabla^s \mathbf{u}) \mathbf{n} = \mathbf{r} \quad \text{on } \Gamma_i, \tag{2.25}$$

$$(-p\mathbf{I} + 2\mu \nabla^s \mathbf{u}) \mathbf{n} = \mathbf{0} \quad \text{on } \Gamma_o. \tag{2.26}$$

Second, we obtain the adjoint problem by taking the derivative of the Lagrangian (2.6) with respect to the state variables $(\mathbf{u}, p, \mathbf{r})$. The adjoint problem then reads as

$$\begin{aligned} \mathcal{P}_{adj}(\mathbf{u}, \tilde{\mathbf{u}}^t): \text{ for } \tilde{\mathbf{u}}^t \text{ and } \mathbf{u}, \text{ solution of (2.21)–(2.26),} \\ \text{determine } (\lambda_u, \lambda_p, \lambda_r) \in \mathcal{U} \times L^2(\Omega) \times \mathbf{H}^{-1/2}(\Gamma_i) \text{ such that} \\ \left\langle \frac{\partial \mathcal{L}}{\partial \mathbf{u}}, \hat{\mathbf{u}} \right\rangle = \int_{\Gamma_o \cup \Gamma_i} [\alpha (\chi_{\Gamma_{so}} + \chi_{\Gamma_{si}})(\mathbf{u} - \tilde{\mathbf{u}}^t) \cdot \hat{\mathbf{u}}] \, d\Gamma - \int_{\Gamma_i} (\lambda_r \cdot \hat{\mathbf{u}}) \, d\Gamma \\ + \int_{\Omega} [\alpha \chi_{\Omega_s} (\mathbf{u} - \tilde{\mathbf{u}}^t) \cdot \hat{\mathbf{u}} + \rho(\nabla \hat{\mathbf{u}}) \mathbf{u} \cdot \lambda_u + \rho(\nabla \mathbf{u}) \hat{\mathbf{u}} \cdot \lambda_u \\ + 2\mu \nabla^s \hat{\mathbf{u}} \cdot \nabla^s \lambda_u - \lambda_p \operatorname{div} \hat{\mathbf{u}}] \, d\Omega = 0, \quad \forall \hat{\mathbf{u}} \in \mathcal{U}, \end{aligned} \tag{2.27}$$

$$\left\langle \frac{\partial \mathcal{L}}{\partial p}, \hat{p} \right\rangle = - \int_{\Omega} \hat{p} \operatorname{div} \lambda_u \, d\Omega = 0, \quad \forall \hat{p} \in L^2(\Omega), \tag{2.28}$$

$$\left\langle \frac{\partial \mathcal{L}}{\partial \mathbf{r}}, \hat{\mathbf{r}} \right\rangle = - \int_{\Gamma_i} \hat{\mathbf{r}} \cdot \boldsymbol{\lambda}_u \, d\Gamma = 0, \quad \forall \hat{\mathbf{r}} \in \mathbf{H}^{-1/2}(\Gamma_i), \tag{2.29}$$

where we considered the following indicator functions:

$$\chi_{\Omega_s} = \begin{cases} 1 & \text{in } \Omega_s, \\ 0 & \text{in } \Omega \setminus \Omega_s, \end{cases} \quad \chi_{\Gamma_{si}} = \begin{cases} 1 & \text{in } \Gamma_{si}, \\ 0 & \text{in } \Gamma_i \setminus \Gamma_{si}, \end{cases} \quad \chi_{\Gamma_{so}} = \begin{cases} 1 & \text{in } \Gamma_{so}, \\ 0 & \text{in } \Gamma_o \setminus \Gamma_{so}. \end{cases} \tag{2.30a-c}$$

Application of standard variational arguments for (2.27)–(2.29) delivers the associated Euler–Lagrange equations, as follows:

$$\alpha \chi_{\Omega_s} (\mathbf{u} - \tilde{\mathbf{u}}^t) - \rho(\nabla \boldsymbol{\lambda}_u) \mathbf{u} + \rho(\nabla \mathbf{u})^T \boldsymbol{\lambda}_u - \mu \Delta \boldsymbol{\lambda}_u + \nabla \lambda_p = \mathbf{0} \quad \text{in } \Omega, \tag{2.31}$$

$$\operatorname{div} \boldsymbol{\lambda}_u = 0 \quad \text{in } \Omega, \tag{2.32}$$

$$\boldsymbol{\lambda}_u = \mathbf{0} \quad \text{on } \Gamma_w, \tag{2.33}$$

$$\boldsymbol{\lambda}_u = \mathbf{0} \quad \text{on } \Gamma_i, \tag{2.34}$$

$$\alpha \chi_{\Gamma_{si}} (\mathbf{u} - \tilde{\mathbf{u}}^t) + (-\lambda_p \mathbf{I} + 2\mu \nabla^s \boldsymbol{\lambda}_u) \mathbf{n} = \boldsymbol{\lambda}_r \quad \text{on } \Gamma_i, \tag{2.35}$$

$$\alpha \chi_{\Gamma_{so}} (\mathbf{u} - \tilde{\mathbf{u}}^t) + \rho(\mathbf{u} \cdot \mathbf{n}) \boldsymbol{\lambda}_u + (-\lambda_p \mathbf{I} + 2\mu \nabla^s \boldsymbol{\lambda}_u) \mathbf{n} = \mathbf{0} \quad \text{on } \Gamma_o. \tag{2.36}$$

Finally, let us compute the optimality condition, which states

$\mathcal{P}_{opt}(\boldsymbol{\lambda}_r)$: for $\boldsymbol{\lambda}_r$, solution of (2.31)–(2.36), determine $\mathbf{g} \in \mathbf{H}_{00}^{1/2}(\Gamma_i)$ such that

$$\left\langle \frac{\partial \mathcal{L}}{\partial \mathbf{g}}, \hat{\mathbf{g}} \right\rangle = \int_{\Gamma_i} [\beta \mathbf{g} \cdot \hat{\mathbf{g}} + \beta_1 \nabla_{\boldsymbol{\tau}} \mathbf{g} \cdot \nabla_{\boldsymbol{\tau}} \hat{\mathbf{g}} + \boldsymbol{\lambda}_r \cdot \hat{\mathbf{g}}] \, d\Gamma = 0, \quad \forall \hat{\mathbf{g}} \in \mathbf{H}^{1/2}(\Gamma_i). \tag{2.37}$$

The Euler–Lagrange equations associated with (2.37) are the following:

$$\beta \mathbf{g} - \beta_1 \Delta_{\boldsymbol{\tau}} \mathbf{g} = -\boldsymbol{\lambda}_r \quad \text{on } \Gamma_i, \tag{2.38}$$

$$\mathbf{g} = \mathbf{0} \quad \text{on } \gamma_i, \tag{2.39}$$

where $\boldsymbol{\lambda}_r$ is solution of the adjoint problem \mathcal{P}_{adj} .

The well-posedness of the fully coupled nonlinear system of necessary conditions given by (2.18)–(2.20), (2.27)–(2.29) and (2.37) has not yet been addressed in the literature to the best of the authors’ knowledge. In this regard, we rely on the well-posedness result reported by Guerra *et al.* (2015) for the minimisation problem expressed in (2.5).

2.3. Gradient descent algorithm

The procedure to solve the optimality conditions at once amounts to solving the nonlinear system of coupled variational equations \mathcal{P}_{sta} , \mathcal{P}_{adj} and \mathcal{P}_{opt} (or their corresponding Euler–Lagrange equations (2.21)–(2.26), (2.31)–(2.36) and (2.38)–(2.39)). This problem is highly nonlinear, and a possible way to find the stationary point for the optimisation problem \mathcal{P}_M is to evaluate the Gâteaux derivative (2.17) to drive a descent-like iterative algorithm. In this case, first, given a guess \mathbf{g} , the forward problem, \mathcal{P}_{sta} , is solved to obtain the state variables, $(\mathbf{u}, p, \mathbf{r})$. Second, the adjoint problem, \mathcal{P}_{adj} , is evaluated using the solution, \mathbf{u} , from the direct problem. Then, using the adjoint variable, $\boldsymbol{\lambda}_r$, obtained from the adjoint problem, the gradient

of the objective function with respect to the parameter \mathbf{g} can be calculated from (2.37) as follows:

$$\frac{D\mathcal{O}(\mathbf{g})}{D\mathbf{g}} = \beta\mathbf{g} - \beta_1\Delta_\tau\mathbf{g} + \lambda_r \quad \text{on } \Gamma_i. \quad (2.40)$$

To ensure an acceptable converging solution of the algorithm, it is usual to start by solving the forward problem based on some initial guess, $(\mathbf{u})_0$, for the flow field. Therefore, we introduce a proper linearisation, \mathcal{P}_{sta}^{lin} , of the forward problem, \mathcal{P}_{sta} , as

$$\begin{aligned} \mathcal{P}_{sta}^{lin}(\mathbf{u}^*, \mathbf{g}^*) : \text{ for } \mathbf{u}^* \text{ and } \mathbf{g}^*, \text{ determine } (\mathbf{u}, p, \mathbf{r}) \text{ such that} \\ \int_{\Omega} [\rho(\nabla\mathbf{u})\mathbf{u}^* \cdot \hat{\lambda}_u + 2\mu\nabla^s\mathbf{u} \cdot \nabla^s\hat{\lambda}_u - p \operatorname{div}\hat{\lambda}_u] d\Omega \\ - \int_{\Gamma_i} \mathbf{r} \cdot \hat{\lambda}_u d\Gamma = 0, \quad \forall \hat{\lambda}_u \in \mathcal{U}, \end{aligned} \quad (2.41)$$

$$- \int_{\Omega} \hat{\lambda}_p \operatorname{div}\mathbf{u} d\Omega = 0, \quad \forall \hat{\lambda}_p \in L^2(\Omega), \quad (2.42)$$

$$- \int_{\Gamma_i} \hat{\lambda}_r \cdot (\mathbf{u} - \mathbf{g}^*) d\Gamma = 0, \quad \forall \hat{\lambda}_r \in \mathbf{H}^{-1/2}(\Gamma_i). \quad (2.43)$$

The optimality condition, (2.37), ensures that the derivative of the objective functional with respect to the control parameters vanishes at the critical point. In the gradient descent algorithm, however, the optimality condition is not satisfied until the algorithm converges. That procedure is described in algorithm 1 below. The fields $(\cdot)^k$ correspond to the fields (\cdot) at the k th iteration. The parameter σ represents the step size, which is adjusted dynamically. To test convergence, a small parameter ξ is prescribed as a tolerance to potentially exit the algorithm, if necessary.

2.4. Numerical methods

The direct and adjoint problems were approximated using the finite volume method. The linearised problem, \mathcal{P}_{sta}^{lin} , was solved using the SIMPLE algorithm described by Patankar & Spalding (1972). According to this, the momentum equation (2.21) is solved (after proper linearisation and discretisation), starting with an initial guess for pressure. In addition, a pressure correction equation is derived from the continuity equation (2.21), obtaining the pressure correction field, which is then used to update both the pressure and the velocity. To solve the discretised momentum equation, we applied the Gauss–Seidel method. Then, the discretised pressure correction equation was solved using a generalised geometric–algebraic multigrid (GAMG) solver using Gauss–Seidel iterations. The adjoint equations (2.31)–(2.36) were discretised and solved in a similar way, following the SIMPLE algorithm and using the same solvers as described for the solution of the direct problem. That is, Gauss–Seidel iterations were used to solve the adjoint momentum equation (2.31) (after its corresponding discretisation) and GAMG was used to solve the discretised adjoint pressure correction derived from the adjoint continuity equation (2.32). The entire optimisation algorithm including the direct and adjoint solvers was implemented using the open source CFD library OpenFOAM (Weller *et al.* 1998).

Algorithm 1 Steepest descent with dynamic step size

Given: $\alpha, \beta, \beta_1 > 0$ ▷ Set optimisation parameters
Input: $\mathbf{u}^0, \mathbf{g}^0, \tilde{\mathbf{u}}^t$ ▷ Provide initial guess and target flow
Output: \mathbf{u}^k ▷ Flow field at last iteration k

1: **procedure** DATAASSIMILATION($\mathbf{u}^0, \mathbf{g}^0, \tilde{\mathbf{u}}^t$)
2: $\sigma \leftarrow 1, \xi \leftarrow 10^{-8}$ and $k \leftarrow 0$
3: $(\mathbf{u}^0, \cdot, \cdot) \leftarrow \mathcal{P}_{sta}^{lin}(\mathbf{u}^0, \mathbf{g}^0)$ ▷ Evaluate linearised problem (2.41)
4: $cost^0 \leftarrow \mathcal{O}^*(\mathbf{u}^0, \mathbf{g}^0, \tilde{\mathbf{u}}^t)$ ▷ Evaluate cost function (2.5)
5: **for** $k \leftarrow 1, n$ **do**
6: $(\cdot, \cdot, \lambda_r^k) \leftarrow \mathcal{P}_{adj}(\mathbf{u}^{k-1}, \tilde{\mathbf{u}}^t)$ ▷ Evaluate adjoint problem (2.27)–(2.29)
7: $s^k \leftarrow -(\beta \mathbf{g}^{k-1} - \beta_1 \Delta_\tau \mathbf{g}^{k-1} + \lambda_r^k)$ ▷ Set steepest descent direction (2.40)
8: **repeat**
9: $\mathbf{g}^k \leftarrow \mathbf{g}^{k-1} + \sigma s^k$ ▷ Update control, using step size σ
10: $(\mathbf{u}^k, \cdot, \cdot) \leftarrow \mathcal{P}_{sta}^{lin}(\mathbf{u}^{k-1}, \mathbf{g}^k)$
11: $cost^k \leftarrow \mathcal{O}^*(\mathbf{u}^k, \mathbf{g}^k, \tilde{\mathbf{u}}^t)$
12: **if** $cost^k \geq cost^{k-1}$ **then**
13: $\sigma \leftarrow 0.5\sigma$
14: **end if**
15: **until** $cost^k < cost^{k-1}$
16: **if** $(|cost^k - cost^{k-1}|)/(cost^k) > \xi$ **then**
17: $\sigma \leftarrow 1.5\sigma$
18: **else**
19: **return** \mathbf{u}^k
20: **end if**
21: **end for**
22: **end procedure**

3. Preprocessing of observational data

The proposed approach was validated and tested based on data that were generated both artificially and empirically. Generated artificial data were used to validate the approach both on a simplified geometry with an available analytical solution (see §4) as well as on a physical glass replica of a human aorta. The latter geometry was used to generate a reference flow solution to be considered as the ground truth for validation purposes (see §5.4). The experimental data were generated with real measurements of flow MRI acquired for the glass replica of the aorta (see §5). Both kinds of observations contain either some artificially added or realistic noise respectively. Hence, the data further require some preprocessing prior to the application of the proposed optimisation algorithm. Let \mathbf{u}_{mri} denote the noisy data, which are either artificially generated or obtained from the MR scan. First of all, a noise detection strategy was applied to the observed data, \mathbf{u}_{mri} , to eliminate potential spurious vectors, yielding a denoised flow field, \mathbf{u}_{mri}^o . Second, the vascular domain was segmented from the (either artificial or experimental) MRI data and was registered with the exact phantom geometry (for both the experimental scenario

with the flow MRI scan and the artificially generated reference flow solution on the phantom). For both artificial and experimental data, the geometries were available as either a user-generated cylinder or the surface data representing the 3-D print of the glass replica respectively. Furthermore, the computational mesh was created from these exact geometries. The measured and denoised velocity field, \mathbf{u}_{mri}° , inside the segmented region of interest was mapped into the computational mesh domain, using the transformation obtained from the registration step. This mapping was performed using linear interpolation, yielding a denoised flow field in the computational mesh domain, denoted as $\bar{\mathbf{u}}_{mri}$. Finally, a space projection was applied to $\bar{\mathbf{u}}_{mri}$ to recover back the divergence-free property of the flow data, which returns a flow field called $\tilde{\mathbf{u}}^*$. The preprocessing steps can be tabularly summarised as follows:

$$\mathbf{u}_{mri} \xrightarrow{\text{outlier detection}} \mathbf{u}_{mri}^\circ \xrightarrow{\text{registration}} \bar{\mathbf{u}}_{mri} \xrightarrow{\text{space projection}} \tilde{\mathbf{u}}^*$$

\mathbf{u}_{mri} : reconstructed flow field from 4-D flow MRI (or artificially generated),

\mathbf{u}_{mri}° : denoised flow field defined in the observational domain (usually coarse mesh),

$\bar{\mathbf{u}}_{mri}$: linearly interpolated flow field mapped in the computational domain (fine mesh),

$\tilde{\mathbf{u}}^*$: divergence-free flow field defined in the computational domain.

3.1. Noise detection

A variation of the usual median test, proposed by Westerweel & Scarano (2005) and initially applied to PIV, was implemented and applied to the MRI data, \mathbf{u}_{mri} , to detect the spurious vectors in the measurements. The method utilises a normalisation to the original median test and considers the local fluctuations of the flow field. For a wide variety of documented flow cases, Westerweel & Scarano (2005) verified the generality of the method for Reynolds numbers ranging from 10^{-1} to 10^7 .

For a more formal description of the method, let us first introduce a set of 3-tuples,

$$N_R = \{(i, j, k) \in \mathbb{Z} \mid -R \leq i, j, k \leq R \wedge R \in \mathbb{N}\} \setminus \{(0, 0, 0)\}. \tag{3.1}$$

Second, we define $\mathbf{U}_x = \mathbf{U}_{x,(0,0,0)} \in \mathbb{R}^n$ to be the displacement vector at pixel position \mathbf{x} , and \mathbf{U}_{x,N_R} is the set of its $[(2R + 1)^3 - 1]$ neighbours. Figure 2 illustrates the neighbourhood for $R = 1$. Additionally, let $\mathbf{U}_{x,med}$ be the median of \mathbf{U}_{x,N_R} . The classical median test value is defined as $(MT)_{x,N_R} = \|\mathbf{U}_{x,med} - \mathbf{U}_x\|$, which is passed if it is smaller than a user-defined threshold value ϵ_t . Furthermore, we define the set of residuals, r_{x,N_R} , as

$$r_{x,N_R} = \{r \in \mathbb{R} \mid r = \|\mathbf{U} - \mathbf{U}_{x,med}\| \wedge \mathbf{U} \in \mathbf{U}_{x,N_R}\}, \tag{3.2}$$

and, similarly, $r_{x,med}$ is defined to be the median of r_{x,N_R} , which is used to normalise the usual median test,

$$(NMT)_{x,N_R} = \frac{\|\mathbf{U}_{x,med} - \mathbf{U}_x\|}{r_{x,med} + \epsilon} < \epsilon_t. \tag{3.3}$$

Under uniform flow conditions, the main normalisation factor $r_{x,med}$ tends to yield zero; hence, a small and acceptable local fluctuation level ϵ is applied to compensate for a potential division by zero and to account for remaining velocity fluctuations obtained from cross-correlation analysis. In practice, ϵ values between 0.1 and 0.2 might be used (Westerweel & Scarano 2005; Raffel *et al.* 2007; Garcia 2011). In our

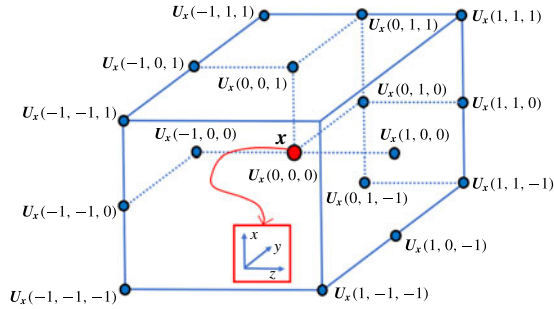


FIGURE 2. (Colour online) For $R = 1$, the set U_{x,N_1} is shown with the 26 neighbours of U_x (not all neighbours illustrated). It should be noted that N_R does not contain the tuple $(0, 0, 0)$; hence, $U_x = U_{x,(0,0,0)}$ is not included in U_{x,N_1} .

case, $\epsilon = 0.2$ performed well for the available MR flow data. Furthermore, $\epsilon_t = 2.25$ is used as the validation threshold. Once the latter parameter is detected from numerical experiments, it can be used for other data in similar flow regimes with the same imaging modality.

Prior to the application of noise detection, the observations \mathbf{u}_{mri} obtained from MRI measurements are initially already divergence-free. This is ensured by the constraints applied during the reconstruction process of the MRI data, which is out of the scope of this work. After denoising, however, the detected spurious vectors are erased from the data, which results in a flow field \mathbf{u}_{mri}° with gaps at certain positions within the observations. This clearly violates the divergence-free property of the observed data \mathbf{u}_{mri} . One possible way to fill in the gaps would be the use of some interpolation scheme. However, such schemes will not necessarily ensure a solenoidal flow field. Therefore, we rely on the application of a projection over a divergence-free space at a later stage (see § 3.4) to automatically fill in the aforementioned gaps and to recover back the divergence-free property of the flow field.

3.2. Segmentation and registration

After the removal of outliers, the arterial structures, in which the analysis is to be performed, are segmented from both the artificially generated flow data as well as the acquired MR measurements. The experimental MRI data comprise the anatomical structures and the velocity field data (Markl *et al.* 2012), whereas the artificial flow data consist of the flow field generated either in a cylindrical geometry or in the geometry of the phantom aorta. For validation studies in the simplified domain, the flow data were used for segmentation of the cylindrical geometry (see § 4), whereas for experimental and complementary validation studies, the anatomical data from MR images were used to extract the vascular geometry from the aorta replica (see § 5). The segmentation was performed using the snake evolution method available in ITK-SNAP (<http://www.itksnap.org>) and was smoothed using the tools available in the VMTK library (<http://www.vmtk.org>). This procedure is expected to suffer from the low resolution and partial volume effects of flow MRI data.

For the comparison with experimental MRI data, high-resolution aortic surface data were already available from the 3-D print of the glass replica. The latter were used to generate the computational mesh for the exact geometry. However, after image acquisition and segmentation, the flow data are misaligned with the exact geometry

of the replica. Therefore, a registration step was necessary to align the measured flow field with the exact geometry of the replica. The rigid registration was performed using the iterative closest point (ICP) algorithm, which aims to minimise the distance between two sets of points. The numbers of available points in the point clouds of both the exact and the segmented geometries were approximately 1600 000 and 12 000 respectively. Prior to the registration process, 5000 points were randomly sampled from each geometry, which were then used as the two point input clouds for the ICP algorithm. The root-mean-square error between the registered point clouds was 0.001. In the case of the artificially generated flow data in the cylindrical domain, no registration step was required, since the geometry was already aligned with the segmented domain.

3.3. Mapping in the computational mesh

For both cases, the analytical geometry (cylinder) and the experimental geometry (glass replica of aorta), the available exact geometries were used to generate the computational mesh domain, which was used for the flow simulations. For both datasets, a hexahedral mesh was created using OpenFOAM's snappyHexMesh procedure. In the case of the experimental geometry, the mesh was rigidly transformed into its corresponding segmentation using the mapping obtained from the registration step. After mesh generation, the velocities, \mathbf{u}_{mri}^o , from the denoised phase difference images (obtained from 4-D flow MRI and denoised with the universal outlier detection scheme) with limited resolution (i.e. in a coarse observational domain) were mapped into the fine hexahedral mesh (computational domain for CFD simulations with high resolution) using the linear interpolation method available in ITK (Johnson *et al.* 2013). As a result of the combination of the linear interpolation and the previous noise detection process, the final flow field (denoted by $\bar{\mathbf{u}}_{mri}$) in the CFD mesh was not divergence-free. The divergence-free property was then recovered with the projection over a divergence-free space applied to the velocity field in the CFD mesh, as explained next.

3.4. Projection into divergence-free space

Let $\bar{\mathbf{u}}_{mri} \in (L^2(\Omega))^3$ be a given observation, projected into a bounded Lipschitz domain $\Omega \in \mathbb{R}^3$ with boundary $\partial\Omega$. According to Helmholtz–Hodge decomposition (HHD), the velocity field can be decomposed into the sum of its divergence-free, curl-free and gradient of harmonic components, if the velocity is known at the boundary (Denaro 2003; Harouna & Perrier 2012; Bhatia *et al.* 2013). In this work, we reconstruct the divergence-free flow field by removing the gradient of the harmonic component and solving the following problem:

$$\left. \begin{aligned} \mathcal{P}_\perp(\bar{\mathbf{u}}_{mri}) : \text{ given } \bar{\mathbf{u}}_{mri}, \text{ find } \tilde{\mathbf{u}}^* = \bar{\mathbf{u}}_{mri} - \nabla q \text{ such that} \\ \Delta q = \nabla \cdot \bar{\mathbf{u}}_{mri} \text{ in } \Omega \\ q = 0 \text{ on } \Gamma_w \text{ and } \nabla q \cdot \mathbf{n} = 0 \text{ on } \partial\Omega \setminus \Gamma_w. \end{aligned} \right\} \quad (3.4)$$

The problem \mathcal{P}_\perp differs from the HHD in terms of the applied BCs, but under certain modifications the HHD can be recovered. Although the problem \mathcal{P}_\perp does not directly correspond to the HHD, it still represents a projection over a space of divergence-free flow fields.

The observations, $\bar{\mathbf{u}}_{mri}$, are assumed to be already modified by the application of the universal outlier detection scheme (as described in § 3.1) prior to its projection in the

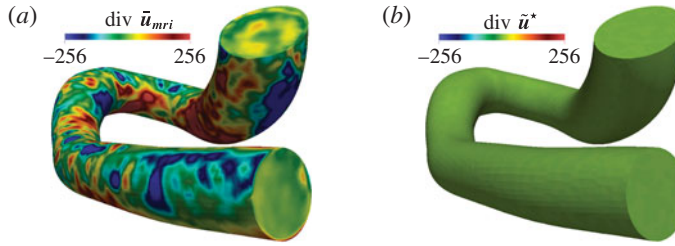


FIGURE 3. (Colour online) The divergence of the flow field in a phantom of a human aorta acquired with MRI: (a) raw data, before the application of the divergence-free projection operator, \mathcal{P}_\perp ; (b) the divergence-free flow field, after the application of \mathcal{P}_\perp .

CFD mesh. The projection ($\mathbf{u}_{mri}^\circ \rightarrow \bar{\mathbf{u}}_{mri}$) is performed by linear interpolation. Problem \mathcal{P}_\perp is solved using OpenFOAM's (Weller *et al.* 1998) conjugate gradient solver (PCG) with simplified diagonal-based incomplete Cholesky preconditioner (DIC). Figure 3 illustrates that the projection into the space of divergence-free vector fields (in the phantom replica of the human aorta) recovers the divergence-free property of the flow field to a great extent.

4. Validation of the methodology

To validate the approach and analyse its performance, we consider the flow of a fluid in a cylindrical geometry, where an analytical solution of a fully developed flow is available. In this work, first an analytical solution is generated for a fine hexahedral mesh of a cylinder. Second, a much coarser voxel grid is used to simulate the MRI acquisition pipeline. For each voxel, the MRI simulation is based on the averaged velocity field provided by the fine mesh. Furthermore, some artificial noise is added to the voxel data and, finally, these artificially generated MRI data are put into the preprocessing pipeline described in § 3.

4.1. Poiseuille flow

We consider the fully developed laminar flow of a Newtonian fluid in a cylinder of length L , constant cross-sectional area A and diameter D ($R = D/2$ is the pipe radius). The solution of the Navier–Stokes equations in this case yields

$$\mathbf{u}_{ext}(r) = \frac{\Delta P D^2}{16\nu\rho L} \left(1 - \frac{r^2}{R^2}\right). \quad (4.1)$$

From (4.1), and calling U_{avr} the average velocity, it can be derived that $\mathbf{u}_{ext}(r) = 2U_{avr}(1 - r^2/R^2)$. Finally, taking $Re = DU_{avr}/\nu$, the analytical solution can be given in terms of the Reynolds number and kinematic viscosity as

$$\mathbf{u}_{ext}(r) = \frac{2\nu Re}{D} \left(1 - \frac{r^2}{R^2}\right). \quad (4.2)$$

4.2. Evaluation of analytical solution

During the MRI acquisition process, the velocities are spatially averaged. To simulate such a framework, the exact solution from (4.2) needs to be spatially averaged to the

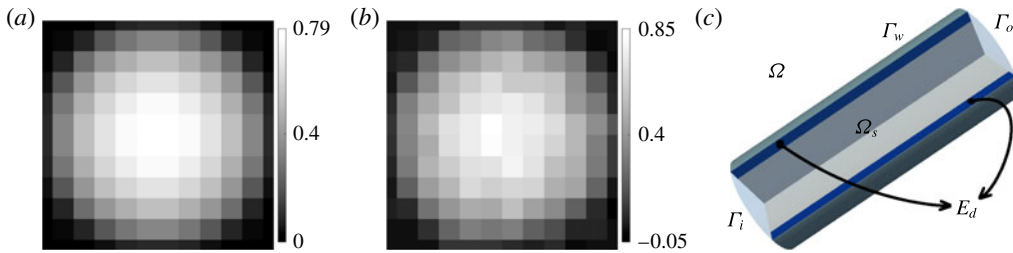


FIGURE 4. (Colour online) Artificially generated velocity images (2 mm isotropic voxel size) of both (a) the exact solution and (b) the integrated noise with an SNR of 20, before their mapping into (c) the computational flow domain.

desired MRI voxel size. Since it is not possible to calculate the exact solution for an infinite number of points, its evaluation was performed on each cell centre of a fine hexahedral mesh with 3693 600 cells. The cylinder radius was $R = 1.2$ cm (diameter $D = 2.4$ cm) and the length was $L = 6$ cm (see figure 4c). As the solution described by the Hagen–Poiseuille equation (4.1) is valid for laminar flow, the Reynolds number was chosen to be 2000. Finally, as a reasonable approximation of blood viscosity in the human aorta, the kinematic viscosity was chosen to be $\nu = 4.8$ cP. Under these conditions, the maximum flow velocity in the aforementioned cylinder approximately results in $|\mathbf{u}|_{max} \approx 0.8$ m s⁻¹.

4.3. Generation of artificial MRI data

The acquired velocities with flow MRI are proportional to the phase shift in the signal of spins moving along a magnetic gradient field. Since the phase of a signal is limited to 2π radians, so is also the range of velocities that can be detected uniquely. The highest velocity that is likely to be encountered within the region of interest is held within a user-defined velocity encoding (VENC). For velocity magnitudes higher than the VENC, the so-called velocity aliasing effect (or phase wrap-around artefact) occurs, which prevents the unique assignment of the velocities. The quality of flow MRI suffers from velocity noise, which is proportional to the velocity encoding and inversely associated with the signal-to-noise ratio (SNR) in the related phase difference images (Pelc *et al.* 1991). As described by Pelc *et al.* (1991), the standard deviation of the velocity can be approximated as

$$\sigma_u \approx (0.45 * \text{VENC}) / \text{SNR}. \quad (4.3)$$

Gudbjartsson & Patz (1995) showed that in the existence of noise, the image intensity in phase-contrast MRI is governed by the Rician distribution. For SNR greater than two, the noise distribution is shown to be nearly Gaussian. The analytical solution evaluated in the fine mesh was first averaged into an MRI grid of 2 mm voxel size in each direction, as shown in figure 4(a). Gaussian white noise was added thereafter on the averaged velocities, as shown in figure 4(b). The VENC was chosen to be 120 cm s⁻¹ in the longitudinal direction (z), whereas it was 20 cm s⁻¹ in the remaining directions (x and y). The standard deviation of the velocity was chosen such that the noise amplitude corresponded to an SNR of 20. As the cylinder is user-defined, the acquired flow field is already registered with the exact geometry. After the addition of artificial noise, the thus-simulated MRI data follow the preprocessing pipeline (with

the exception of the registration stage), as described in § 3, before starting the CFD simulation. In what follows, \mathbf{u}_{snr} will represent the noisy MRI measurements, which are mapped into the computational domain and for which a decomposition is applied to project the field over a divergence-free space, as described in §§ 3.3 and 3.4. The cylindrical computational domain is illustrated in figure 4(c).

4.4. Optimisation with exact solution as target flow

First, we consider one case where the optimisation starts with a noisy flow field and is performed against the exact solution. That is, the target flow field $\tilde{\mathbf{u}}^t$ in the objective function (2.5) corresponds to \mathbf{u}_{ext} given by (4.2). In addition, the initial condition, $(\mathbf{u})_0 = \mathbf{u}^0$, corresponds to the artificially generated divergence-free flow field, \mathbf{u}_{snr} , as described in § 4.3. Thus, algorithm 1 is executed with the input parameters $(\mathbf{u}_{snr}, \mathbf{g}_{snr}, \mathbf{u}_{ext})$, where $\mathbf{g}_{snr} = \mathbf{u}_{snr}$ on Γ_i . In what follows, we will denote $\mathbf{u}_{opt} = \mathbf{u}_{opt}^k$ as the solution returned by the optimisation process after k iterations of algorithm 1. The mesh is set up with 118 800 cells including 114 840 hexahedras and 3960 prisms. The size of the mesh is suitable to obtain satisfactory results. Flow-matching domains, Ω_s , Γ_{si} and Γ_{so} (see figure 4c), cover the lumen, including both inlet and outlet boundaries. In what follows, we will give a meaning to the subscript, s , in the flow-matching domain, Ω_s . The subscript s prescribes the extent of contraction of the whole domain Ω in millimetres (mm), as follows:

$$\Omega_s = \{\mathbf{x} \in \Omega \mid \|\mathbf{x} - \mathbf{y}\| \geq s(\text{mm}) \forall \mathbf{y} \in \Gamma_w\}. \tag{4.4}$$

In this set-up, we set $s = 2$. That is, the flow-matching domain Ω_s is a contracted domain of Ω such that the distance to Γ_w is at least 2 mm. Figure 4(c) shows the example of Ω_s in the cylinder. Furthermore, the optimisation parameters are $\alpha = 0.15$, $\beta = 10^{-4}$ and $\beta_1 = 10^{-8}$. Figure 5(a–c) illustrates the norms of the flow matching, $\|\tilde{\mathbf{u}}^t - \mathbf{u}\|_{fm}$, the control, $\|\mathbf{g}\|_{co}$, and the surface gradient of the control, $\|\nabla_{\tau} \mathbf{g}\|_{sg}$, which are defined as follows:

$$\|\tilde{\mathbf{u}}^t - \mathbf{u}\|_{fm} = \left(\frac{100}{\text{avr}_{\Omega} |\tilde{\mathbf{u}}^t|} \right) \sqrt{\frac{1}{V_{\Omega}} \int_{\Omega} |\tilde{\mathbf{u}}^t - \mathbf{u}|^2 d\Omega}, \tag{4.5}$$

$$\|\mathbf{g}\|_{co} = \left(\frac{1}{\text{avr}_{\Gamma_i} |\tilde{\mathbf{u}}^t|} \right) \sqrt{\frac{1}{A_{\Gamma_i}} \int_{\Gamma_i} |\mathbf{g}|^2 d\Gamma}, \tag{4.6}$$

$$\|\nabla_{\tau} \mathbf{g}\|_{sg} = \left(\frac{1}{\text{avr}_{\Gamma_i} |\nabla_{\tau} \tilde{\mathbf{u}}^t|} \right) \sqrt{\frac{1}{A_{\Gamma_i}} \int_{\Gamma_i} |\nabla_{\tau} \mathbf{g}|^2 d\Gamma}, \tag{4.7}$$

where V_{Ω} is the volume of the entire domain and A_{Γ_i} is the area at the inlet. The norms are normalised against the average magnitude of the target velocity or its surface gradient.

As can be seen in figure 5(b), the norm of the control, $\|\mathbf{g}\|_{co}$, rapidly grows at the beginning, forcing the noisy vectors towards their desired position and remaining almost constant after a while. In figure 5(c), the sudden decrease in the norm of the velocity surface gradient, $\|\nabla_{\tau} \mathbf{g}\|_{sg}$, shows the denoising process at the inlet. Once a good approximation is reached, the velocities at the inlet are only being adjusted

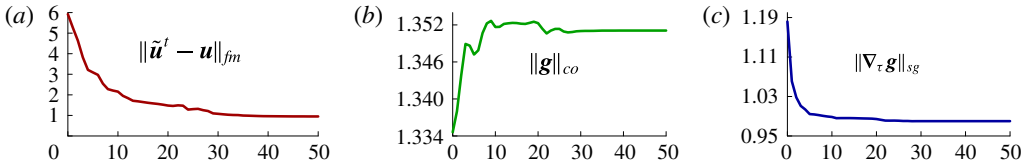


FIGURE 5. (Colour online) The norms from optimisation with parameters $\alpha = 0.15$, $\beta = 10^{-4}$ and $\beta_1 = 10^{-8}$. The norms are plotted against the number of iterations on the horizontal axis. (a) Flow matching, (b) control, (c) surface gradient of control.

slightly during the rest of the iterations. This is continued until a sufficient flow matching is achieved in the entire domain, as illustrated in figure 5(a).

Let us now focus on the results in the domain close to the cylinder wall. To confirm the presented results also with respect to the accuracy in the near-wall regions, we calculated both the root-mean-square error, $\text{nRMSE}_d = \text{nRMSE}_d(\mathbf{u}_{\text{ext}}, \mathbf{u}_{\text{opt}})$, and the flow direction error, $\text{FDE}_d = \text{FDE}_d(\mathbf{u}_{\text{ext}}, \mathbf{u}_{\text{opt}})$, defined by

$$\text{nRMSE}_d(\mathbf{u}_t, \mathbf{u}_c) = \left(\frac{100}{\text{avr}|\mathbf{u}_t|} \right) \sqrt{\frac{1}{V_d} \int_{E_d} |\mathbf{u}_t - \mathbf{u}_c|^2 dE_d}, \quad (4.8)$$

$$\text{FDE}_d(\mathbf{u}_t, \mathbf{u}_c) = \sqrt{\frac{1}{V_d} \int_{E_d} \left(1 - \frac{\mathbf{u}_t \cdot \mathbf{u}_c}{|\mathbf{u}_t||\mathbf{u}_c|} \right)^2 dE_d}. \quad (4.9)$$

In what follows, the subscript d stands for the evaluation of the error within the contracted subdomain $E_d \subset \Omega$ with volume V_d , which is defined as

$$E_d = \{\mathbf{x} \in \Omega \mid \exists \mathbf{y} \in \Gamma_w, \|\mathbf{x} - \mathbf{y}\| < d \text{ (mm)}\}. \quad (4.10)$$

That is, we want to evaluate the errors in the domain E_d at near-wall regions (this domain is not meant to be included in the flow-matching domain Ω_s), where the nearest Euclidean distance of all points in E_d is at most d mm apart from the wall, Γ_w . Figure 4(c) features the contracted domain in the cylinder. It should be noted that both errors, (4.8) and (4.9), are evaluated between the exact solution, \mathbf{u}_{ext} , and the results obtained from the proposed optimisation strategy, \mathbf{u}_{opt} , in the contracted region E_d . In addition, the error nRMSE_d is normalised against the average velocity magnitude of the observations in E_d .

For $d = 2$, the initial errors $\text{nRMSE}_2(\mathbf{u}_{\text{ext}}, \mathbf{u}_{\text{snr}})$ and $\text{FDE}_2(\mathbf{u}_{\text{ext}}, \mathbf{u}_{\text{snr}})$ between the exact solution, \mathbf{u}_{ext} , and noisy observations, \mathbf{u}_{snr} , were 26.65% and 1.1×10^{-2} respectively. After optimal control, the root-mean-square error, as a percentage of the average velocity magnitude, was reduced to $\text{nRMSE}_2(\mathbf{u}_{\text{ext}}, \mathbf{u}_{\text{opt}}) = 3.53\%$, and the flow direction error was $\text{FDE}_2(\mathbf{u}_{\text{ext}}, \mathbf{u}_{\text{opt}}) = 3.5 \times 10^{-5}$.

4.4.1. Sensitivity analyses with respect to changes in optimisation parameters

There have been some reported discussions in the literature concerning the choice of the optimisation parameters for related control problems, mostly based on simplified 2-D geometries. In Lee (2011), the penalisation value was set to 10^{-10} for a Neumann boundary control and validations were performed for a flow problem in a 2-D square case. In Guerra, Tiago & Sequeira (2014), a 2-D geometry for a stenosed vessel was

considered, where the parameter related to the surface gradient term (denoted as β_1 in this work) was set to 10^x , with $x \in \{-5, -4, -2, -1, 0, 1\}$, whereas the other optimisation parameters were maintained constant. Further works have also reported on the choice of regularisation parameters in the related field (Fursikov, Gunzburger & Hou 1998; D'Elia *et al.* 2012a; Bertagna *et al.* 2014; Guerra *et al.* 2015).

In this work, the parameter α was chosen on a trial and error basis. It was observed that α should be between 0.15 and 0.5 depending on the data being used. Values larger than 0.5 enforce a more stringent flow matching, and the optimiser already stops at very early stages of the iterations. For values smaller than 0.15, the optimiser performs more iterations because the flow-matching term is more relaxed. In the latter case, as expected, the final solution gets further away from the observations.

The differences in the response as a consequence of changes in the optimisation parameters, β and β_1 , were examined in this work for the 3D case. First of all, we set $\alpha = 0.15$, which was experimentally found to be an appropriate parameter for this use case and was then used in the sensitivity analyses with respect to changes in β and β_1 . Second, we kept $\beta_1 = 10^{-8}$ fixed and modified β . Figure 6(a,b) shows the flow-matching norm, $\|\tilde{\mathbf{u}}^t - \mathbf{u}\|_{fm}$, and the control norm, $\|\mathbf{g}\|_{co}$, for different β values. In addition, figure 6(b) also contains the constant norm, $\|\mathbf{g}_{ext}\|_{co}$, of the exact solution. We observed that for larger values, such as $\beta > 10^{-4}$, there was not enough control and the flow matching was poor. This is because the objective function was rapidly penalised at early stages of the optimisation, where the optimiser needs larger controls in order to reduce the error. For smaller β values, however, there was no hard penalisation and the optimiser could apply larger controls, as illustrated in figure 6(b). In general, the values 10^{-4} and 10^{-5} delivered satisfactory results, and $\beta = 10^{-5}$ was observed to be the best choice. Furthermore, we fixed β at 10^{-5} and ran the optimiser with β_1 set to 10^{-7} , 10^{-8} and 10^{-9} (smaller values of β_1 rendered unacceptable solutions because of the lack of smoothing effect on noisy measurements). For different β_1 values, figure 7(a,c) shows the plots for the flow-matching norm, $\|\tilde{\mathbf{u}}^t - \mathbf{u}\|_{fm}$, and the surface gradient norm, $\|\nabla_{\tau} \mathbf{g}\|_{sg}$. Let us first analyse the results between the values 10^{-7} and 10^{-8} for β_1 . It can be observed that the norm of the surface gradient is further reduced for $\beta_1 = 10^{-8}$ over the successive iterations, and better flow matching is achieved. This can be explained by further investigation of the control norm, $\|\mathbf{g}\|_{co}$, along with the norm of the exact solution, $\|\mathbf{g}_{ext}\|_{co}$, in figure 7(b). We can observe that there is not enough control for $\beta_1 = 10^{-7}$. This shows that even if we are able to remove the noise at the inlet (which is explained by the reduction in the value of the surface gradient for $\beta_1 = 10^{-7}$), the controls are small and hence the velocities cannot be properly controlled. Second, let us consider the results for β_1 values of 10^{-8} and 10^{-9} . Figure 7(a) shows that the flow matching is achieved with an almost equally good quality. In figure 7(b), however, fluctuations along the iterations can be observed in the norm of controls for $\beta_1 = 10^{-9}$. In addition, figure 7(c) shows that the fluctuations also have an effect on the norm of the surface gradient, which is not as greatly reduced in early iterations as is the case for $\beta_1 = 10^{-8}$. Finally, our interpretations are also confirmed quantitatively in near-wall regions. Table 1 summarises the results from the sensitivity analysis comparing the root-mean-square errors, nRMSE₂, and the flow direction errors, FDE₂, for varied optimisation parameters. Our conclusion is that a value of $\beta_1 = 10^{-8}$ delivers sufficiently accurate results, and this value will be used hereafter.

4.5. Optimisation with noisy solution as target flow

So far, we have been able to validate the proposed approach using an analytical solution. Actually, an exact solution is not available or cannot be provided by

(β, β_1)	$(10^{-3}, 10^{-8})$	$(10^{-4}, 10^{-8})$	$(10^{-5}, 10^{-8})$	$(10^{-5}, 10^{-9})$	$(10^{-5}, 10^{-7})$
$\text{nRMSE}_2(\mathbf{u}_{ext}, \mathbf{u}_{opt})$	4.53 %	3.53 %	3.41 %	3.68 %	8.40 %
$\text{FDE}_2(\mathbf{u}_{ext}, \mathbf{u}_{opt})$	7.0×10^{-5}	3.5×10^{-5}	2.8×10^{-5}	1.4×10^{-4}	4.8×10^{-5}

TABLE 1. Dimensionless root-mean-square ($\text{nRMSE}_2(\mathbf{u}_{ext}, \mathbf{u}_{opt})$) and flow direction ($\text{FDE}_2(\mathbf{u}_{ext}, \mathbf{u}_{opt})$) errors measured within the near-wall (2 mm) domain (E_2).

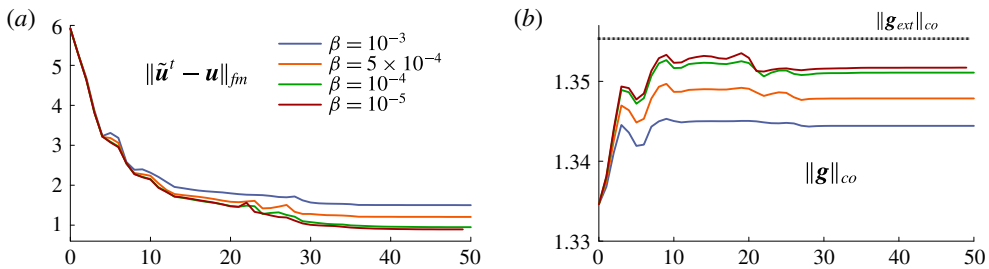


FIGURE 6. (Colour online) Alteration in norms of (a) flow matching and (b) control (solid lines in a,b) with respect to changes in β , along with the constant norm of the exact solution (dashed line in b), where $\alpha = 0.15$ and $\beta_1 = 10^{-8}$. The norms are plotted against the number of iterations on the horizontal axis.

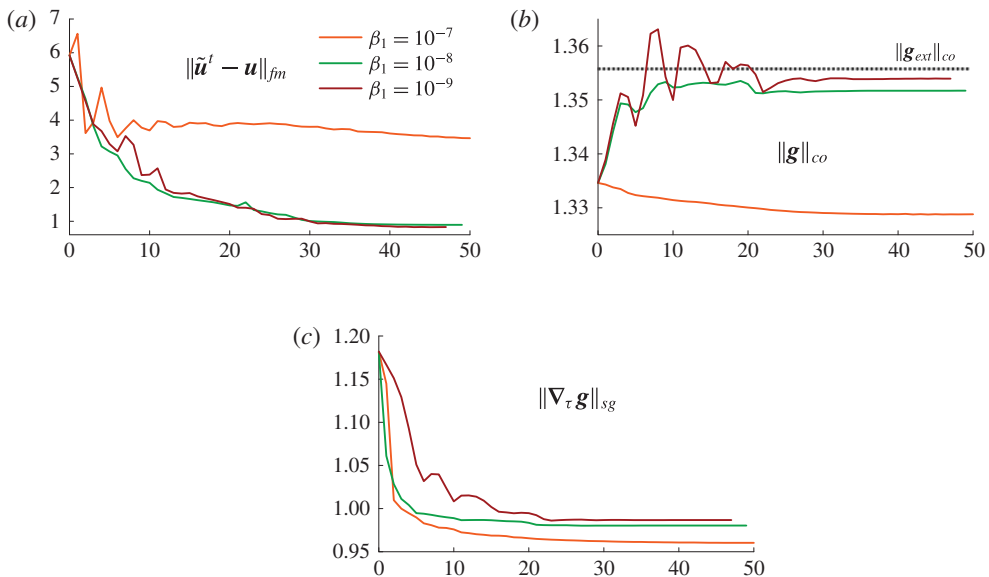


FIGURE 7. (Colour online) Alteration in norms of (a) flow matching, (b) control and (c) control surface gradient (solid lines in a-c) with respect to changes in β_1 , along with the constant norm of the exact solution (dashed line in b), where $\alpha = 0.15$ and $\beta = 10^{-5}$. The norms are plotted against the number of iterations on the horizontal axis.

measurements or experiments. Here, the performance of the optimisation framework was evaluated considering the artificially generated noisy measurements as the

target flow. That is, we set $\tilde{\mathbf{u}}^f = \mathbf{u}_{snr}$ in the objective function (2.5). In order to avoid lack of control, the initial flow field was low-pass filtered with a cutoff frequency of 0.5. The low-pass filtered field is just a smoothed version of the measurements. It reduces the edge contents and results in a blurred image. The degree of the smoothness is proportional to the chosen cutoff frequency. Use of a blurred (smoothed or low-pass filtered) version of the measurements as initial condition is not mandatory. However, the motivation behind using it was the fact that, preferably, the flow-matching term in the objective function (first term in (2.5)) should not result in a null value at the very first iteration (e.g. by the application of the measurements directly as initial condition). Moreover, the choice of such an initial condition enables us to start with a guess close (in some sense) to the measurements (as opposed to the case of, e.g., potentially applying a zero field as initial condition) to avoid a significantly large number of iterations until the convergence. The resulting flow field is represented by \mathbf{u}_{lpf} in Ω , and algorithm 1 was executed with the input parameters $(\mathbf{u}_{lpf}, \mathbf{g}_{lpf}, \mathbf{u}_{snr})$, where $\mathbf{g}_{lpf} = \mathbf{u}_{lpf}$ on Γ_i . Motivated by the findings of the previous section, parameters β and β_1 were set to 10^{-5} and 10^{-8} respectively. As before, the flow matching was performed in Ω_s with $s = 2$. The parameter α was adjusted to 0.5 for this set-up. Under these conditions, the quantitative results yielded 4.85% and 5.8×10^{-5} for nRMSE₂ and FDE₂ respectively.

4.5.1. Sensitivity analyses with respect to changes in the flow-matching domain

As described in §4.3, the addition of artificial noise follows the same procedure at each location in the flow domain and does not depend on the velocity magnitudes. Hence, the near-wall regions with very low velocities contain almost no relevant signal, but mostly noise. Moreover, near-wall regions also contain further errors due to partial volume effects. Hence, such locations should rather be avoided in the flow-matching domain, Ω_s . Therefore, a further contraction in the subdomain was considered in addition. To account for it, we performed a sensitivity analysis with respect to changes in the flow-matching domain Ω_s using the same parameters as specified above. The simulations were performed with s varying from 1.5 to 4.

The norms of the control are shown in figure 8(a) for different values of s . It can be observed that larger controls result for $s = 2.5$. The magnitude of the control \mathbf{g} decreases if Ω_s is further contracted or extended. This can be also confirmed by nRMSE_{*d*} in figure 8(b), where the x -axis represents s . The errors in near-wall regions are further decreased for $s = 2.5$. In addition, figure 8(b) illustrates the error measurements (y -axis) for different values of d represented in different colours. It can be observed that in all cases, the optimisation framework delivers accurate results at locations of the domain close to the lateral boundary (the wall). This is especially interesting for the evaluation of WSSs, some of the most important parameters for diagnostic purposes in the cardiovascular field. Table 2 summarises the results in the near-wall domains E_d defined for different distances from the wall (with d values ranging from 3 mm to 0.5 mm) for varying flow-matching domains Ω_s with s varying from 1.5 to 4. For example, for a flow-matching domain $\Omega_{2.5}$, which is 2.5 mm apart from the wall Γ_w , the root-mean-square error nRMSE₂, which is evaluated within 2 mm distance of the wall Γ_w , is 4.52%, and FDE_{0.5} is 5.0×10^{-5} . This improves the accuracy in comparison with the results from the previous section, where the flow-matching domain was chosen to be Ω_2 . For $s \geq 3$, the accuracy also starts to drop. This is a remarkable finding for the choice of Ω_s . In addition, contraction of the flow-matching domain also in the longitudinal direction (e.g. exclusion of the locations at and near the inlet/outlet boundaries from Ω_s) also results in loss of accuracy. In

s	1.5	2	2.5	3	3.5	4
nRMSE ₃	5.92 %	4.86 %	4.46 %	4.90 %	5.85 %	7.26 %
FDE ₃	6.1×10^{-5}	4.8×10^{-5}	4.2×10^{-5}	4.4×10^{-5}	4.7×10^{-5}	5.0×10^{-5}
nRMSE ₂	5.85 %	4.85 %	4.52 %	4.92 %	5.86 %	7.35 %
FDE ₂	7.5×10^{-5}	5.8×10^{-5}	5.0×10^{-5}	5.3×10^{-5}	5.7×10^{-5}	6.0×10^{-5}
nRMSE ₁	6.03 %	5.18 %	4.97 %	5.29 %	5.98 %	7.36 %
FDE ₁	1.0×10^{-4}	7.9×10^{-5}	6.9×10^{-5}	7.3×10^{-5}	7.7×10^{-5}	8.2×10^{-5}
nRMSE _{0.5}	6.68 %	5.93 %	5.88 %	6.18 %	6.64 %	7.80 %
FDE _{0.5}	1.3×10^{-4}	1.0×10^{-4}	8.7×10^{-5}	9.2×10^{-5}	9.8×10^{-5}	1.0×10^{-4}

TABLE 2. Dimensionless root-mean-square (nRMSE _{d} (\mathbf{u}_{ext} , \mathbf{u}_{opt})), and flow direction (FDE _{d} (\mathbf{u}_{ext} , \mathbf{u}_{opt})), errors measured within the near-wall (d (mm)) domain, E_d , for varying flow-matching domains Ω_s (s (mm)) apart from the wall).

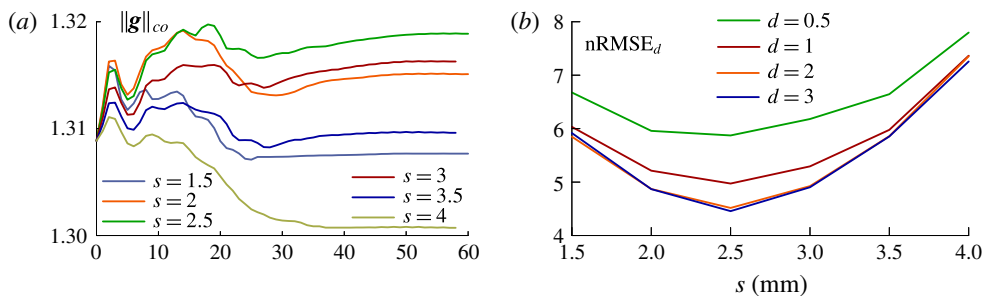


FIGURE 8. (Colour online) Illustration of (a) norms of control (for different s) with respect to changes in the flow-matching domain, Ω_s , and (b) root-mean-square errors (plotted against s for different d) in the near-wall domain, E_d . The norms are plotted against the number of iterations in the horizontal axis.

this case, the errors (achieved from the contractions in the longitudinal direction) increase to a similar extent to that already given in table 2 for the radial contractions. In general, the flow-matching domain should be constructed such that it contains almost all available information about the flow field in the luminal area (reaching from inlet to outlet), whereas it should avoid using the information at near-wall locations. We have shown that it is a very good choice to keep the flow-matching domain 2.5 (mm) away from the vessel wall for this case.

4.5.2. Comparison against classical CFD

Finally, the ability of the boundary control approach to the measured flow field in the entire domain was compared against the results delivered from the classical CFD strategy. The latter is based on a single forward simulation, with Dirichlet BCs, applied (as usual) at the inlet boundary. Then, the classical CFD implies solution of the problem \mathcal{P}_{sta} , as stated by the variational equations (2.18)–(2.20). Thus, using the initial guess \mathbf{u}_{snr} and the BC $\mathbf{u} = \mathbf{u}_{snr}$ on Γ_i , the linearised problem $\mathcal{P}_{sta}^{lin}(\mathbf{u}_{snr}, \mathbf{g}_{snr})$ was solved with $\mathbf{g}_{snr} = \mathbf{u}_{snr}$ on Γ_i , iteratively until convergence was achieved. In what follows, the solution obtained from a classical CFD approach will be denoted as \mathbf{u}_{cf} . Motivated by the conclusion in §4.5.1, the optimisation algorithm was employed to deliver the optimised solution \mathbf{u}_{opt} for parameters $\alpha = 0.5$, $\beta = 10^{-5}$, $\beta_1 = 10^{-8}$ and $s = 2.5$. Furthermore, the optimisation was performed against the noisy solution as

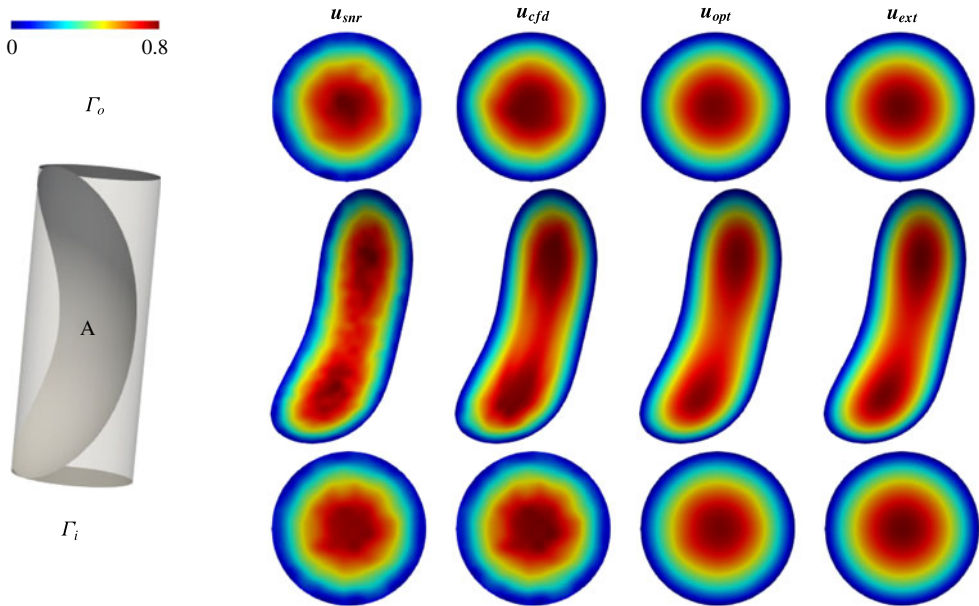


FIGURE 9. (Colour online) Flow patterns for the fields \mathbf{u}_{snr} , \mathbf{u}_{cfd} , \mathbf{u}_{opt} and \mathbf{u}_{ext} illustrated at the inlet (Γ_i), the outlet (Γ_o) and a curved surface (A) immersed in the lumen. The colours representing the velocity magnitudes are scaled to the range of 0 and 0.8, whereas the corresponding maximum velocities are $|\mathbf{u}_{snr}|_{max} \approx 0.853$, $|\mathbf{u}_{cfd}|_{max} \approx 0.777$, $|\mathbf{u}_{opt}|_{max} \approx 0.784$ and $|\mathbf{u}_{ext}|_{max} \approx 0.8$.

target flow and initialised with the low-pass filtered flow field, as described in §4.5. We want to emphasise that, during the optimisation procedure, there is no knowledge available about the exact solution at all.

Flow patterns were first inspected visually to obtain a qualitative interpretation. Figure 9 shows the flow patterns in the domain, obtained from the artificially generated noisy measurements, \mathbf{u}_{snr} , the computations via the traditional CFD method, \mathbf{u}_{cfd} , the computations from the proposed optimisation framework, \mathbf{u}_{opt} , and finally the exact solution, \mathbf{u}_{ext} . It can be appreciated that the optimised flow is the one that better resembles the exact solution. Especially, it features excellent qualitative agreement with the exact solution at the inlet boundary and at locations near to the inlet, where the traditional CFD approach suffers from inaccuracy, caused by the noisy BC.

To confirm the previous qualitative assessment, the simulation results from both the classical CFD and the control approaches were quantitatively compared against the exact solution. First, we evaluated $nRMSE_d$ and FDE_d in the near-wall domain E_d for the values $d = 2$, $d = 1$ and $d = 0.5$. Table 3 shows that the velocity field was reconstructed by the optimisation algorithm much more accurately at the wall boundary, in comparison with the classical CFD approach. Noisy observations, \mathbf{u}_{snr} , deliver almost no relevant signal near the boundaries, which can be observed by the huge and increasing errors for decreasing d values. In contrast, however, $nRMSE_d$ is more rapidly decreased when applying the optimisation algorithm to obtain \mathbf{u}_{opt} , as we get closer to wall boundary. This shows the feasibility of the optimisation approach, especially for its accuracy at the boundaries. Furthermore, the flow direction errors are decreased to a much greater extent for the optimised flow in comparison with the classical CFD method. This also shows clearly that the noise at the inlet boundary

$x = \mathbf{u}_{ext}$	nRMSE $_d(\mathbf{x}, \mathbf{y})$			FDE $_d(\mathbf{x}, \mathbf{y})$		
	$\mathbf{y} = \mathbf{u}_{snr}$	$\mathbf{y} = \mathbf{u}_{cfd}$	$\mathbf{y} = \mathbf{u}_{opt}$	$\mathbf{y} = \mathbf{u}_{snr}$	$\mathbf{y} = \mathbf{u}_{cfd}$	$\mathbf{y} = \mathbf{u}_{opt}$
$d = 2$	26.65 %	8.36 %	4.52 %	1.1×10^{-2}	1.2×10^{-3}	5.0×10^{-5}
$d = 1$	61.30 %	11.79 %	4.97 %	1.6×10^{-2}	1.7×10^{-3}	6.9×10^{-5}
$d = 0.5$	139.82 %	17.93 %	5.88 %	2.1×10^{-2}	2.1×10^{-3}	8.7×10^{-5}

TABLE 3. Dimensionless root-mean-square (nRMSE $_d(\mathbf{u}_{ext}, \mathbf{y})$) and flow direction (FDE $_d(\mathbf{u}_{ext}, \mathbf{y})$) errors for $\mathbf{y} = \{\mathbf{u}_{snr}, \mathbf{u}_{cfd}, \mathbf{u}_{opt}\}$, measured within the near-wall (d mm) domain (E_d). Optimisation is performed using measurements in the flow-matching volume (Ω_s), which is $s = 2.5$ mm apart from the wall boundary.

is removed to a great extent by the application of the control. In addition, it can be seen that FDE $_d$ is not further decreased as we get close to the walls. This is expected, since the optimisation procedure itself is a trade-off between decreasing the flow-matching errors in terms of magnitudes and the flow direction errors based on the surface gradient. Both terms are included in the objective function and are affected by the choice of parameters.

In addition, the computational cost of both the classical CFD method and the optimisation procedure were evaluated and compared in terms of wall clock time (or execution time). The classical CFD method using the SIMPLE algorithm required approximately 100 iterations to reach the solution, and its execution time was 34 s. In turn, the data assimilation process required approximately 50 iterations with an execution time of 82 s.

Finally, the maximum and average WSSs were calculated from the numerical results based on the classical CFD and the optimisation procedure. These quantities were then compared against the WSSs computed with the analytical solution. Figure 10 shows the box plots to characterise the discrepancies between the WSS field obtained from the exact solution, \mathbf{u}_{ext} , and the WSS fields obtained from both the computations with classical CFD, \mathbf{u}_{cfd} , and the optimised solution, \mathbf{u}_{opt} .

5. Data assimilation in a realistic geometry

The proposed approach was tested for the flow-matching control problem in a more realistic geometry obtained from a glass replica of a human aorta. The geometry consisted of aortic root, ascending aorta, aortic arch without branches and descending aorta, as illustrated in figure 1(a). First, a validation study was performed on the aorta based on a manufactured solution used as the ground truth. The results from the assimilation procedure and the classical CFD method were quantitatively compared against the ground truth (available reference solution). Second, real flow data were gathered from the flow MRI scans to investigate the performance of the solvers in real case scenarios. The optimisation results were first qualitatively compared with measured data. In addition, and since there is no reference solution available in this case, the results were quantitatively compared against the results when using the classical CFD method prescribing Dirichlet BCs. The discrepancies between the solution obtained from the data assimilation approach and the CFD solution were also examined in contrast to the discrepancies encountered between both solutions in the manufactured scenario involving the aorta phantom geometry. Furthermore, a sensitivity analysis with respect to changes in the initial guess flow field was analysed and discussed in the real case scenario. Finally, the proposed approach was tested

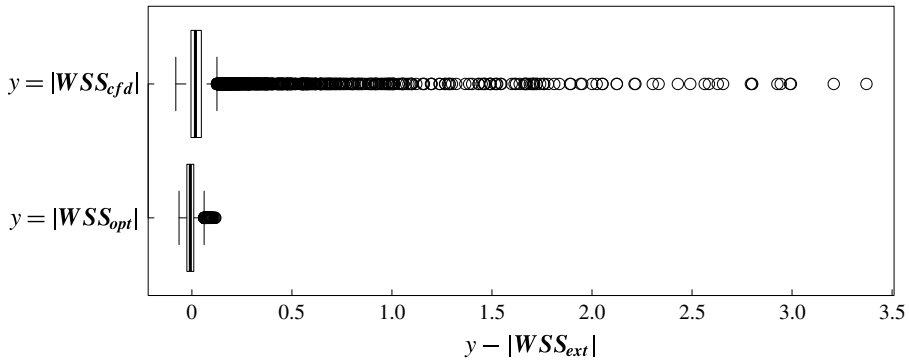


FIGURE 10. Box plot illustrating the differences ($|WSS_{cfd}| - |WSS_{ext}|$) and ($|WSS_{opt}| - |WSS_{ext}|$) on the horizontal axis, where the labels WSS_{cfd} , WSS_{opt} and WSS_{ext} represent the wall shear stresses corresponding to the fields u_{cfd} , u_{opt} and u_{ext} respectively.

under flow conditions with increasing Reynolds numbers ranging approximately from 1200 up to 2100. For the highest Reynolds number, a mesh sensitivity analysis was also carried out.

5.1. Experimental set-up

The *in vitro* experiment was prepared in a scanner and control room including a 3T MRI scanner from Philips. The glass replica, covered by a six-element cardiac coil, was placed in the scanner and connected to a centrifugal pump (in the control room) with a maximum pressure of 3.9 bar. The connection was made with a PVC tubing of total length 20 m with an inner diameter of 19 mm. The inlet and outlet of the pipe were connected to a reservoir in the control room, creating an open circuit. A ball bearing valve was placed 1.5 m downstream of the tube and was used to control the flow rate. Figure 11 illustrates the experimental set-up.

The reservoir was filled with a mixture of 24 l H_2O , 40 g carboxymethyl cellulose carboxymethyl (CMC) and 10 g sulphate. The aim of the CMC medium was to increase the viscosity of the fluid to an approximately similar level to blood viscosity. On the other hand, the sulphate acted as a contrast agent to increase the signal magnitude. For a temperature of 27° C, the mixture featured a viscosity of 3.5 cP.

Three different image acquisitions were performed to obtain data with increasing Reynolds numbers. The maximum velocities in the obtained data were 1.06, 1.71 and 2.26 $m s^{-1}$, and the corresponding Reynolds numbers were 1223, 1860 and 2105 respectively. Thus, the flow rates were controlled such that the obtained data contained laminar flow. We highlight the fact that the flow model does not account for turbulence, and consideration of turbulence models is matter of current research.

A 3-D spoiled gradient-echo sequence with flow encoding gradients was used for the flow MRI acquisitions. The eddy-current induced background phase was compensated by application of linear phase correction. The acquisition parameters were chosen as flip angle 10°, time of repetition and echo (TR/TE) 2.6/4.87 ms, field of view (FOV) $[244 \times 244 \times 62] mm^3$ and voxel size $[1.4 \times 1.4 \times 1.5] mm^3$. Furthermore, considering the increasing Reynolds numbers of the measured data, the corresponding VENCs were chosen as 120, 200 and 260 $cm s^{-1}$ respectively.

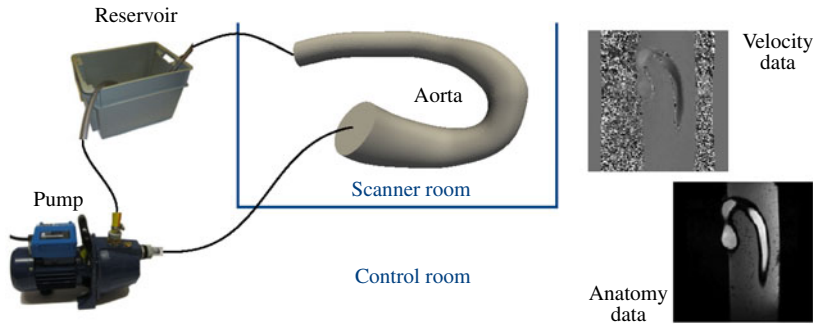


FIGURE 11. (Colour online) The experimental set-up for the glass replica of a human aorta.

5.2. On the imaging resolution of flow MRI

Flow MRI is primarily limited by the SNR, and the scanning parameters must be chosen such that there is a trade-off between the acquisition time and the spatial/temporal resolution. Besides, in patient-specific cardiovascular acquisition, the optimised scan parameters must take the variability of the cardiac period and/or shifts in patient position into account and ensure that physiological artefacts, such as respiratory motion, are minimised (Callaghan & Grieve 2016). A substantial decrease in the voxel size is not clinically feasible. This would increase the scan time (potentially by several hours), which is not practical for a patient lying inside the MRI device. At the same time, this will result in a lower number of protons within the voxel substantially decreased in size. Hence, the gathered signal will suffer more from noise and the SNR will decrease.

Under normal clinical conditions, it is currently possible to acquire a 4-D flow dataset of the heart and major vessels in approximately 10 min at a spatial resolution of 2.5 mm (isotropic) with a temporal resolution of 30–40 ms (Callaghan *et al.* 2016). In the work reported by Bock *et al.* (2011), the authors used 2.1 mm isotropic voxel size for patient-specific measurement of the aorta. In addition, Cibis *et al.* (2015) performed MRI scans of fontant patients using a spatial resolution of $1.9\text{--}2.5 \times 1.9\text{--}2.5 \times 2.2\text{--}3.3 \text{ mm}^3$ with coverage of the heart and large arteries. Further studies have performed personalised acquisitions of the ventricle based on a cross-sectional resolution between 1.9 and 2.5 mm (de Vecchi *et al.* 2016; Larsson *et al.* 2017). However, the most recent studies of flow MRI have investigated the feasibility towards even higher resolutions with clinically feasible scan times. Schmitter *et al.* (2016) reported increased imaging resolutions, such of 1.2 mm isotropic voxel size, using accelerated protocols.

Following the clinical feasibility and considering the recent improvements in terms of the resolution, we have therefore used an approximately 1.5 mm isotropic voxel size in our acquisitions, which finally resulted in a resolution of $1.4 \times 1.4 \times 1.5 \text{ mm}^3$.

5.3. Data preprocessing

For the generation of the computational mesh, the aortic replica was first segmented (see figure 12a) from the anatomical data and then smoothed (see figure 12b). Thereafter, the available exact geometry (see figure 12d), with the region of interest that defines the inlet/outlet boundaries highlighted, was registered with the smoothed

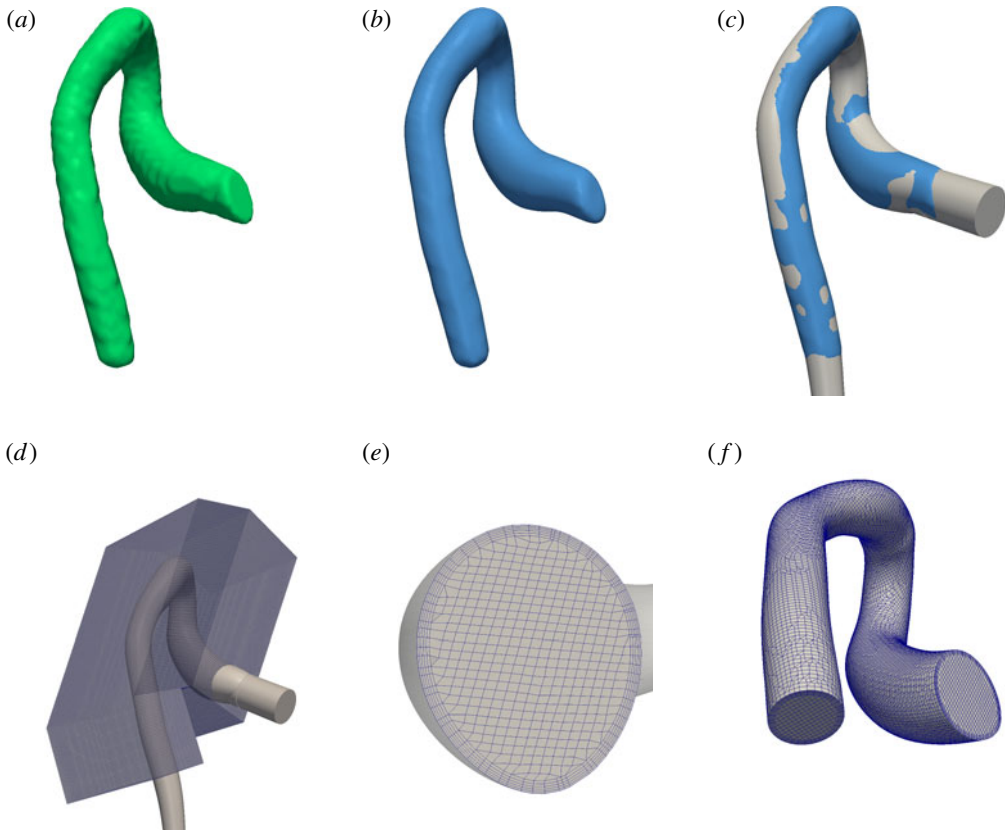


FIGURE 12. (Colour online) Mesh generation from (d) the exact geometry including (a) the segmentation of the domain from anatomical data, (b) smoothing and (c) registration of the exact geometry with the smoothed geometry. A region of interest (d) defines the computational domain for which a hexahedral mesh with 122 079 cells is created, shown in (e) at the inlet and (f) in the domain.

geometry, as shown in figure 12(c). Section 3.2 provides more details about the applied segmentation and registration. Finally, a hexahedral mesh with 122 079 cells was created using the exact geometry cut by the region of interest. Moreover, two additional hexahedral meshes with approximately 750 000 and 1 370 000 cells were created for a mesh sensitivity analysis. Figure 12(e–f) illustrates the computational mesh with 122 079 cells.

Having generated the computational mesh, the measured flow data followed into the preprocessing pipeline, as described in §3. In what follows, \mathbf{u}_{smr}^{Re} with $Re = \{1223, 1860, 2105\}$ will represent the flow fields derived after the application of divergence-free space projection; that is, after solving the problem \mathcal{P}_\perp described by the equation (3.4).

5.4. Validation of the data assimilation based on a manufactured solution in the aorta

Due to the noisy nature of flow MRI scans, there exists no true reference solution in such real case scenarios. This makes it difficult to posit an argumentation about the

value of the assimilation procedure. Therefore, we have first generated a numerical reference solution on the computational mesh to validate the approach on the aortic geometry. The numerical solution will be considered as the ground truth in the quantification of the errors.

The generation of the ground truth was based on a forward steady-state flow simulation with an idealised BC at the inlet, resembling a parabolic flow profile. A kinematic viscosity of 4.5 cP was considered and the resulting flow field with $Re = 1780$ had a maximum flow velocity of 0.8 m s^{-1} . In what follows, the ground truth will be denoted as \mathbf{u}_{ext} . An artificial noise with an isotropic VENC of 0.9 m s^{-1} and an SNR of 10 (see § 4.3 for more details) was added on top of the ground truth. Following our usual notation, the noisy flow field (after being decomposed into its divergence-free components) will be denoted as \mathbf{u}_{snr} .

To analyse the performance of the optimisation procedure for such a realistic aortic geometry, the assimilation was first performed against the ground truth. Thus, the target flow in the objective function (2.5) was set as $\tilde{\mathbf{u}}^t = \mathbf{u}_{ext}$ and algorithm 1 was executed with the input parameters $(\mathbf{u}_{snr}, \mathbf{g}_{snr}, \mathbf{u}_{ext})$, where $\mathbf{g}_{snr} = \mathbf{u}_{snr}$ on Γ_i . The resulting flow field will be denoted as \mathbf{u}_{opt}^{ext} in the sense of the solution of data assimilation performed against the ground truth. A quantitative comparison of the assimilation procedure directly against the ground truth in terms of $\text{nRMSE}_d(\mathbf{u}_{opt}^{ext}, \mathbf{u}_{ext})$ yielded 0.8, 1.1 and 1.4 % for $d = 2, 1, 0.5$ respectively. The errors are relatively small, and this shows the feasibility of the approach in a complex geometry.

However, in a real case scenario, a ground truth is usually not available and the assimilation cannot be performed against an already known solution. In order to avoid any bias in favour of one of the solvers (the optimisation or the classical CFD), the assimilation was additionally performed against the noisy solution. That is, algorithm 1 was additionally executed with the input parameters $(\mathbf{u}_{snr}, \mathbf{g}_{snr}, \mathbf{u}_{snr})$. In this case, the resulting flow field will be denoted as \mathbf{u}_{opt}^{snr} . The classical CFD method was also executed, where the Dirichlet BC and the initial conditions were set to the flow field \mathbf{u}_{snr} , and the resulting flow field will be denoted as \mathbf{u}_{cf} . In this sense, both solvers have no information whatsoever about the ground truth prior starting the simulations. The errors, $\text{nRMSE}_1(\mathbf{x}, \mathbf{u}_{ext})$ and $\text{FDE}_1(\mathbf{x}, \mathbf{u}_{ext})$, evaluated for $\mathbf{x} = \{\mathbf{u}_{cf}, \mathbf{u}_{opt}^{snr}, \mathbf{u}_{opt}^{ext}\}$, were 6.81 %, 4.77 %, 1.10 % and 0.12, 0.10, 0.01 respectively. This reveals that the optimisation solver still performs better in comparison with the classical CFD method, even if one assimilates against a noisy solution. The rather small difference between 6.81 % and 4.77 % can be explained by the fact that the errors within the close proximity of the wall are evaluated in the entire domain. However, it should be noted that in this aorta geometry the size of the entire domain is much larger than the region where the BCs have a true impact. Indeed, after the development length, whatever the BC is, the solution tends to become that of a fully developed flow, and the errors are masked by this fact. In other words, as the optimisation controls the velocities at the inlet, it is expected that more representative errors are encountered near the inlet location. To investigate this, the same errors were evaluated near the aortic root inlet (within a close proximity of the inlet), instead of taking the entire domain. Let us define a further contracted subdomain domain $E_d^s \subset E_d \subset \Omega$ as follows:

$$E_d^s = \{\mathbf{x} \in \Omega \mid \exists \mathbf{y} \in \Gamma_w, \exists \mathbf{z} \in \Gamma_i, \|\mathbf{x} - \mathbf{y}\| < d \text{ (mm)} \wedge \|\mathbf{x} - \mathbf{z}\| < s \text{ (mm)}\}. \quad (5.1)$$

Correspondingly, the errors nRMSE_d^4 and FDE_d^4 are defined within 4 cm proximity of the inlet in the corresponding domain E_d^4 and will be used in the rest of this work.

$x \rightarrow$	\mathbf{u}_{cfd}	\mathbf{u}_{opt}^{snr}	\mathbf{u}_{opt}^{ext}	$d \rightarrow$	2	1	0.5
$nRMSE_1^4(\mathbf{x}, \mathbf{u}_{ext})$	34 %	17 %	5 %	$nRMSE_d^4(\mathbf{u}_{cfd}, \mathbf{u}_{opt}^{snr})$	23 %	30 %	34 %
$FDE_1^4(\mathbf{x}, \mathbf{u}_{ext})$	0.22	0.18	0.03	$FDE_d^4(\mathbf{u}_{cfd}, \mathbf{u}_{opt}^{snr})$	0.11	0.13	0.15

TABLE 4. On the left, root-mean-square errors ($nRMSE_1^4(\mathbf{x}, \mathbf{u}_{ext})$) and flow direction errors ($FDE_1^4(\mathbf{x}, \mathbf{u}_{ext})$) evaluated within the close proximity (4 cm) of the inlet and the near-wall (1 mm) domain (E_1^4), where $\mathbf{x} = \{\mathbf{u}_{cfd}, \mathbf{u}_{opt}^{snr}, \mathbf{u}_{opt}^{ext}\}$. On the right, the corresponding errors $nRMSE_d^4(\mathbf{u}_{cfd}, \mathbf{u}_{opt}^{snr})$ and $FDE_d^4(\mathbf{u}_{cfd}, \mathbf{u}_{opt}^{snr})$ reporting the difference between the solutions of the classical CFD, \mathbf{u}_{cfd} , and the data assimilation procedure, \mathbf{u}_{opt}^{snr} .

The errors, $nRMSE_1^4(\mathbf{x}, \mathbf{u}_{ext})$ and $FDE_1^4(\mathbf{x}, \mathbf{u}_{ext})$, evaluated for $\mathbf{x} = \{\mathbf{u}_{cfd}, \mathbf{u}_{opt}^{snr}, \mathbf{u}_{opt}^{ext}\}$, were 34 %, 17 %, 5 % and 0.22, 0.18, 0.03 respectively. These results are also summarised on the left-hand side of table 4. It can be observed that, compared with the results of the classical CFD method, there is a significant improvement in the outcome provided by the assimilation (against the noisy solution) in the close proximity of the inlet. This is a remarkable finding for the improvement of the flow field, especially at the aortic root, which is a place where flow disturbances can easily lead to pathological modifications of the arterial wall.

Furthermore, we examined the difference between the solutions of the optimisation, \mathbf{u}_{opt}^{snr} , and the classical CFD, \mathbf{u}_{cfd} . The errors, $nRMSE_1^4(\mathbf{u}_{cfd}, \mathbf{u}_{opt}^{snr})$ and $FDE_1^4(\mathbf{u}_{cfd}, \mathbf{u}_{opt}^{snr})$, were 23 %, 30 %, 34 % and 0.11, 0.13, 0.15 respectively. Thus, the difference between the data assimilation procedure and the classical CFD method is approximately 30 %, which clearly emphasises to what extent the data assimilation is able to alter the CFD solution. The right-hand side of table 4 summarises the differences between the two solvers.

5.5. Numerical results based on flow MRI scans

We will first present the numerical results for $Re = 1223$ based on the flow data denoted by \mathbf{u}_{snr}^{Re} (as described in § 5.3), mapped on the computational mesh domain and projected into a divergence-free space. In what follows, \mathbf{u}_{snr}^{Re} with $Re = 1223$ will be simply denoted as \mathbf{u}_{snr} . The target flow in the objective function (2.5) was set as $\tilde{\mathbf{u}}^t = \mathbf{u}_{snr}$. A low-pass filtered flow field of this target flow with a cutoff frequency of 4 was used as the initial guess, which will be denoted as $(\mathbf{u})_0 = \mathbf{u}_{lpf}^{4.0}$. The frequency was chosen such that the flow field, being low-pass filtered, was not oversmoothed and remained close to the actual target field. The maximum magnitude of low-pass filtered flow data was 0.98 m s^{-1} , whereas for the target flow it was 1.06 m s^{-1} . Flow matching was performed in Ω_s , with $s = 2.5$, and the optimisation parameters were chosen as $\beta = 10^{-5}$, $\beta_1 = 10^{-6}$ and $\alpha = 0.25$. That is, algorithm 1 was executed in the domain as represented in figure 1(a) with the input parameters $(\mathbf{u}_{lpf}^{4.0}, \mathbf{g}_{lpf}^{4.0}, \mathbf{u}_{snr})$, where $\mathbf{g}_{lpf}^{4.0} = \mathbf{u}_{lpf}^{4.0}$ on Γ_i .

The flow patterns predicted by the optimisation algorithm and the classical CFD method were first qualitatively compared against the measured data by visual inspection. Figure 13 shows the streamlines corresponding to the different velocity fields. Figure 14 illustrates the magnitude of the velocity field in a cross-sectional slice covering part of the ascending and descending aorta. Furthermore, figure 15 highlights the wraps of the velocity profile for a set of transverse slices. It can be observed that the measured velocity field, \mathbf{u}_{snr} , and the optimised solution, \mathbf{u}_{opt} , are

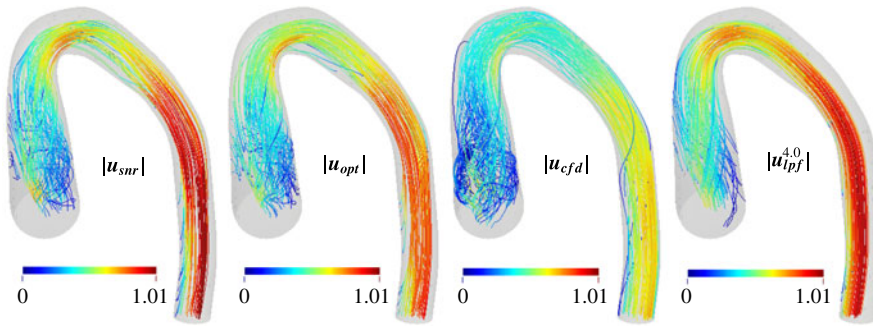


FIGURE 13. (Colour online) Streamlines for the magnitudes of the different velocity fields. The observations considered here are the measured data with $Re = 1223$.

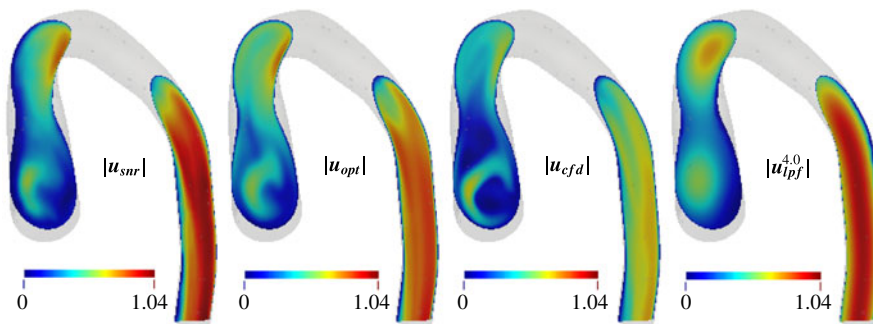


FIGURE 14. (Colour online) Velocity magnitude in a cross-sectional slice for the different velocity fields. The observations considered here are the measured data with $Re = 1223$.

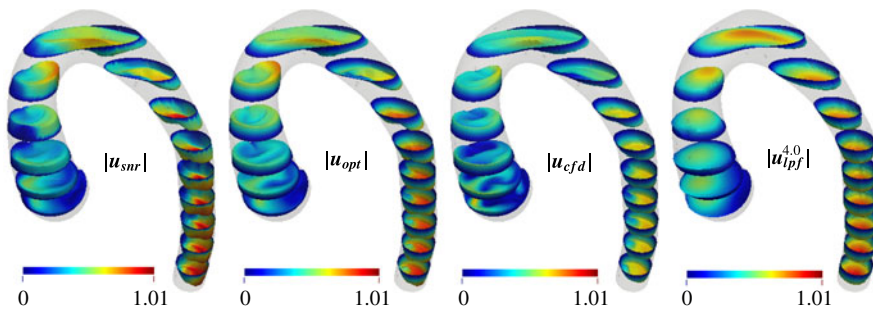


FIGURE 15. (Colour online) Warps of the magnitudes of the velocity fields at a set of cross-sectional slices. The observations considered here are the measured data with $Re = 1223$.

reasonably similar, whereas the flow field predicted by the classical CFD method is relatively far from the measured data.

The results were also analysed quantitatively. However, the observations have a noisy nature and there is no true reference solution available in this case. Respectively, we evaluated the errors between \mathbf{u}_{cfd} and \mathbf{u}_{opt} to quantify the differences of the flow fields predicted by the classical CFD method and the optimisation strategy.

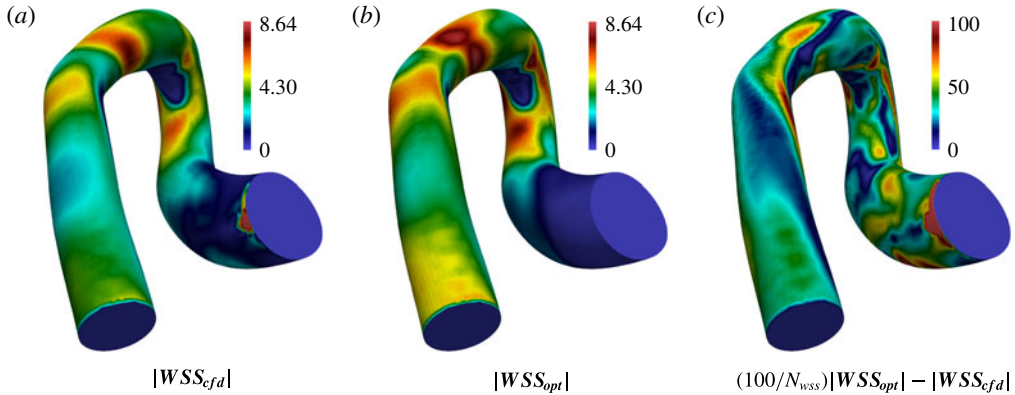


FIGURE 16. (Colour online) (a,b) Magnitude fields of WSSs, $|\mathbf{WSS}_{cfd}|$ and $|\mathbf{WSS}_{opt}|$, corresponding to the velocity fields \mathbf{u}_{cfd} and \mathbf{u}_{opt} . (c) Normalised difference field, $(100/N_{wss})|\mathbf{WSS}_{opt} - \mathbf{WSS}_{cfd}|$ on Γ_w , where N_{wss} is as described in (5.2). The observations considered here are the measured data with $Re = 1223$.

The flow-matching norm, $\|\mathbf{u}_{opt} - \mathbf{u}_{cfd}\|_{fm}$, resulted in 39% of the average velocity magnitude of optimised solution. In addition, the errors were evaluated at the aortic root in the close proximity of the inlet. For $d = \{2, 1, 0.5\}$, the errors $nRMSE_d^4(\mathbf{u}_{cfd}, \mathbf{u}_{opt})$ were 46%, 51% and 60% respectively. This shows that the differences in the predictions grow on getting closer to the wall. The normalised difference, $\|\mathbf{WSS}_{cfd} - \mathbf{WSS}_{opt}\|$ (see (5.2) and (5.3)), between the WSS fields corresponding to the velocity fields \mathbf{u}_{cfd} and \mathbf{u}_{opt} was 43.72%. Furthermore, figure 16(a,b) illustrates the magnitudes of the WSS fields, \mathbf{WSS}_{cfd} and \mathbf{WSS}_{opt} , and figure 16(c) shows their normalised difference field. In addition, figure 17(a,b) illustrates the pressure fields of the predictions from the classical CFD method and from the optimisation strategy respectively, whereas figure 17(c) shows their normalised difference field.

Notably, the better qualitative agreement between the observations and the optimised solution, and quantitatively significant differences between the optimised solution and the predictions from classical CFD, support the fact that the optimisation delivers a better solution when compared with the classical CFD approach. The improvement in the flow field is especially emphasised at the aortic root, which is one of the most important clinically relevant locations for the development of pathological alterations of the anatomical structures underlying the arterial wall,

$$N_{wss} = \frac{1}{A_{\Gamma_w}} \int_{\Gamma_w} \frac{|\mathbf{WSS}_{opt} + \mathbf{WSS}_{cfd}|}{2} d\Gamma, \quad (5.2)$$

$$\|\mathbf{WSS}_{opt} - \mathbf{WSS}_{cfd}\| = \frac{100}{N_{wss}} \sqrt{\frac{1}{A_{\Gamma_w}} \int_{\Gamma_w} |\mathbf{WSS}_{opt} - \mathbf{WSS}_{cfd}|^2 d\Gamma}. \quad (5.3)$$

5.6. Sensitivity with respect to changes in initial guess

To analyse the performance and sensitivity of the optimisation strategy with respect to changes in the initial guess, different flow fields were generated from the observations

Init. guess	$(\mathbf{u})_0 = \mathbf{u}_{snr}$	$(\mathbf{u})_0 = \mathbf{u}_0$	$(\mathbf{u})_0 = \mathbf{u}_{lpf}^{3.5}$	$(\mathbf{u})_0 = \mathbf{u}_{lpf}^{4.0}$	$(\mathbf{u})_0 = \mathbf{u}_{lpf}^{4.5}$
Numb. iters	955	854	640	492	251
$\ \tilde{\mathbf{u}}^t - \mathbf{u}\ _{fm}$	37.17 %	37.01 %	37.03 %	36.84 %	36.91 %
$\text{avr}(\mathbf{WSS}_{opt})$	2.83	2.85	2.85	2.87	2.88

TABLE 5. Results of optimised solutions (number of iterations, flow-matching norm and average WSS) for different initial guesses \mathbf{u}_{snr} , \mathbf{u}_0 , $\mathbf{u}_{lpf}^{3.5}$, $\mathbf{u}_{lpf}^{4.0}$ and $\mathbf{u}_{lpf}^{4.5}$.

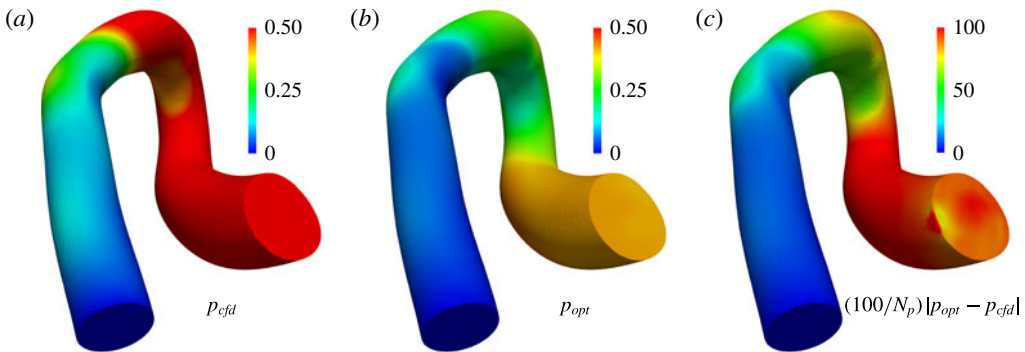


FIGURE 17. (Colour online) Pressure fields corresponding to predictions from classical CFD, p_{cfd} , from optimisation strategy, p_{opt} , and their normalised difference field, $(100/N_p)|p_{opt} - p_{cfd}|$ on $\partial\Omega$, where $N_p = (1/V_\Omega) \int_\Omega (|p_{opt} + p_{cfd}|/2) d\Omega$. The observations considered here are the measured data with $Re = 1223$.

to be applied as the initial guess flow. The observations were low-pass filtered with different cutoff frequencies 3.5 and 4.5, denoted as $\mathbf{u}_{lpf}^{3.5}$ and $\mathbf{u}_{lpf}^{4.5}$ respectively. The maximum velocity magnitude was 1.16 m s^{-1} for the flow field $\mathbf{u}_{lpf}^{3.5}$, whereas it was 0.84 m s^{-1} for $\mathbf{u}_{lpf}^{4.5}$. In addition, a zero flow field, \mathbf{u}_0 , was prepared as the initial guess, that is, $\mathbf{u}_0 = \mathbf{0}$ in Ω . Under the same conditions as in § 5.5, algorithm 1 was executed with input parameters $(\mathbf{u}_{lpf}^{3.5}, \mathbf{g}_{lpf}^{3.5}, \mathbf{u}_{snr})$, $(\mathbf{u}_{lpf}^{4.5}, \mathbf{g}_{lpf}^{4.5}, \mathbf{u}_{snr})$, $(\mathbf{u}_{snr}, \mathbf{g}_{snr}, \mathbf{u}_{snr})$ and $(\mathbf{u}_0, \mathbf{g}_{snr}, \mathbf{u}_{snr})$, where $\mathbf{g}_{lpf}^{3.5} = \mathbf{u}_{lpf}^{3.5}$, $\mathbf{g}_{lpf}^{4.5} = \mathbf{u}_{lpf}^{4.5}$ and $\mathbf{g}_{snr} = \mathbf{u}_{snr}$ on Γ_i correspondingly.

Visual inspection revealed no remarkable differences in the final optimised velocity fields. Table 5 shows the flow-matching norms, the averaged WSS and the number of iterations for the optimisation starting with initial conditions \mathbf{u}_{snr} , \mathbf{u}_0 , $\mathbf{u}_{lpf}^{3.5}$, $\mathbf{u}_{lpf}^{4.0}$ and $\mathbf{u}_{lpf}^{4.5}$ respectively. The numerical experiments with modified initial guesses provide clear evidence that, for the steady-state problem, the data assimilation algorithm is converging to the unique solution of the problem regardless of the initial solution provided. Both the qualitative and the quantitative results indicate that there were no significant changes in the solution with respect to changes in the initial guess provided to the optimisation algorithm. However, the number of iterations to reach convergence was rather sensitive to this initial guess.

5.7. Data assimilation for different Reynolds numbers

In what follows, the measured and preprocessed data will now be denoted as \mathbf{u}_{snr}^{Re} representing the flow fields with different Reynolds numbers, as described in § 5.1. Using the available data with increasing flow rates and setting the initial guesses to

$\mathbf{x} = \mathbf{u}_{cf,d}, \mathbf{y} = \mathbf{u}_{opt}$	$\text{nRMSE}_2^4(\mathbf{x}, \mathbf{y})$	$\text{nRMSE}_1^4(\mathbf{x}, \mathbf{y})$	$\text{nRMSE}_{0,5}^4(\mathbf{x}, \mathbf{y})$
$Re = 1223$, cells: 122 K	46 %	51 %	60 %
$Re = 1860$, cells: 122 K	49 %	58 %	66 %
$Re = 2105$, cells: 122 K	64 %	73 %	80 %
$Re = 2105$, cells: 750 K	53 %	58 %	69 %
$Re = 2105$, cells: 1370 K	46 %	49 %	61 %

TABLE 6. Root-mean-square errors ($\text{nRMSE}_d^4(\mathbf{u}_{cf,d}, \mathbf{u}_{opt})$) and flow direction errors ($\text{FDE}_d^4(\mathbf{u}_{cf,d}, \mathbf{u}_{opt})$) evaluated within the close proximity (4 cm) of the inlet and the near-wall (d mm) domain (E_d^4) for different Reynolds numbers, where $d = \{2, 1, 0.5\}$.

$\mathbf{0}$, algorithm 1 was executed with the input parameters $(\mathbf{0}, \mathbf{g}_{snr}^{Re}, \mathbf{u}_{snr}^{Re})$, where $\mathbf{g}_{snr}^{Re} = \mathbf{u}_{snr}^{Re}$ on Γ_i and $Re = \{1223, 1860, 2105\}$. The results are summarised in table 6. It can be observed that the errors between the solutions predicted by the classical CFD and the optimised flow grow for increasing Reynolds number, and they grow more on getting closer to the wall, which is also consistent with the corresponding validations in table 4 of § 5.4.

For the observed data with $Re = 2105$, the flow field is almost in a transitional region. Therefore, we additionally performed a mesh analysis for the computations relying on the flow field \mathbf{u}_{snr}^{2105} . The consistency of the assimilation on two different additional meshes with 750 000 and 1370 000 cells was examined. Table 6 additionally summarises the errors for the different meshes. In general, it can be observed that the flow field predicted by the classical CFD method diverges by approximately 50 % from the solution provided by the optimised flow.

6. Conclusion

In this work, an optimise-then-discretise approach was developed for the flow control problem using 4-D flow MRI data in the context of computational haemodynamics. The methodology was validated against an analytical solution as well as against experimental MRI measurements performed in a glass replica of a human aorta.

The proposed control algorithm was analysed in detail in order to assess the capabilities of the methodology to reconstruct blood flow in near-wall regions, targeting the computation of haemodynamically relevant quantities such as the wall shear stress.

A critical aspect in the assimilation procedure is the size and location of the domain, Ω_s , where the flow matching is performed. In general, Ω_s should be constructed such that it contains almost all available and reliable information about the flow field in the luminal area (spanning the entire domain from inlet to outlet), whereas it should avoid using the information at near-wall locations.

The method proved to deliver physically consistent flow fields, with substantial reduction of noise present in the 4-D flow MRI measurements, outperforming the predictive capabilities of standard CFD approaches. The proposed approach provides a systematic strategy to improve the model predictions regarding clinically relevant haemodynamic data.

Overall, the flow control algorithm demonstrated robustness and feasibility towards reconstruction of flow fields from partial 4-D flow MRI measurements under different flow regimes with increasing Reynolds number. Reconstruction of the more complex

flow structures observed in transient fluid dynamics and account for turbulence are out of the scope of the present work, and are matters of current research.

The proposed method is the groundwork for the development of a frequency-based approach for periodic flows. Therefore, this study is the first of a sequence that will eventually address the dynamic case.

REFERENCES

- BERTAGNA, L., D'ELIA, M., PEREGO, M. & VENEZIANI, A. 2014 Data assimilation in cardiovascular fluid–structure interaction problems: an introduction. In *Fluid–Structure Interaction and Biomedical Applications* (ed. T. Bodnár, G. P. Galdi & Š. Nečasová), pp. 395–481. Springer.
- BHATIA, H., NORGARD, G., PASCUCCI, V. & BREMER, P. T. 2013 The Helmholtz–Hodge decomposition – a survey. *IEEE Trans. Vis. Comput. Graphics* **19** (8), 1386–1404.
- BOCK, J., FRYDRYCHOWICZ, A., LORENZ, R., HIRTNER, D., BARKER, A. J., JOHNSON, K. M., ARNOLD, R., BURKHARDT, H., HENNIG, J. & MARKL, M. 2011 *In vivo* noninvasive 4D pressure difference mapping in the human aorta: phantom comparison and application in healthy volunteers and patients. *Magn. Reson. Med.* **66** (4), 1079–1088.
- BOUILLOT, P., DELATTRE, B. M., BRINA, O., OUARED, R., FARHAT, M., CHNAFA, C., STEINMAN, D. A., LOVBLAD, K. O., PEREIRA, V. M. & VARGAS, M. I. 2018 3D phase contrast MRI: partial volume correction for robust blood flow quantification in small intracranial vessels. *Magn. Reson. Med.* **79** (1), 129–140.
- CALLAGHAN, F. M. & GRIEVE, S. M. 2016 Spatial resolution and velocity field improvement of 4D-flow MRI. *Magn. Reson. Med.* **78** (5), 1959–1968.
- CALLAGHAN, F. M., KOZOR, R., SHERRAH, A. G., VALLELY, M., CELERMAJER, D., FIGTREE, G. A. & GRIEVE, S. M. 2016 Use of multi-velocity encoding 4D flow MRI to improve quantification of flow patterns in the aorta. *J. Magn. Reson. Imag.* **43** (2), 352–363.
- CAMPBELL, I. C., RIES, J., DHAWAN, S. S., QUYYUMI, A. A., TAYLOR, W. R. & OSHINSKI, J. N. 2012 Effect of inlet velocity profiles on patient-specific computational fluid dynamics simulations of the carotid bifurcation. *Trans. ASME J. Biomech. Engng* **134** (5), 051001.
- CHATZIZISIS, Y. S., COSKUN, A. Ü., JONAS, M., EDELMAN, E. R., FELDMAN, C. L. & STONE, P. H. 2007 Role of endothelial shear stress in the natural history of coronary atherosclerosis and vascular remodeling: molecular, cellular, and vascular behavior. *J. Am. College Cardiol.* **49** (25), 2379–2393.
- CHIU, J.-J. & CHIEN, S. 2011 Effects of disturbed flow on vascular endothelium: pathophysiological basis and clinical perspectives. *Phys. Rev.* **91** (1), 327–387.
- CIBIS, M., JARVIS, K., MARKL, M., ROSE, M., RIGSBY, C., BARKER, A. J. & WENTZELA, J. J. 2015 The effect of resolution on viscous dissipation measured with 4D flow MRI in patients with fontan circulation: evaluation using computational fluid dynamics. *J. Biomech.* **48** (12), 2984–2989.
- CITO, S., PALLARÉS, J. & VERNET, A. 2014 Sensitivity analysis of the boundary conditions in simulations of the flow in an aortic coarctation under rest and stress conditions. In *Statistical Atlases and Computational Models of the Heart. Imaging and Modelling Challenges: STACOM 2013* (ed. O. Camara, T. Mansi, M. Pop, K. Rhode, M. Sermesant & A. Young), Lecture Notes in Computer Science, vol. 8330, pp. 74–82. Springer.
- COLLIS, S. S. & HEINKENSCHLOSS, M. 2002 Analysis of the Streamline Upwind/Petrov Galerkin Method Applied to the Solution of Optimal Control Problems. *Tech. Rep.* TR02–01. Department of Computational and Applied Mathematics, Rice University.
- COUNCIL, NATIONAL RESEARCH 1991 *Four-Dimensional Model Assimilation of Data: A Strategy for the Earth System Sciences*. The National Academies Press.
- D'ELIA, M., MIRABELLA, L., PASSERINI, T., PEREGO, M., PICCINELLI, M., VERGARA, C. & VENEZIANI, A. 2012a Applications of variational data assimilation in computational hemodynamics. In *Modeling of Physiological Flows* (ed. D. Ambrosi, A. Quarteroni & G. Rozza), vol. 5, pp. 363–394. Springer.

- D'ELIA, M., PEREGO, M. & VENEZIANI, A. 2012*b* A variational data assimilation procedure for the incompressible Navier–Stokes equations in hemodynamics. *J. Sci. Comput.* **52** (2), 340–359.
- D'ELIA, M. & VENEZIANI, A. 2010*a* Methods for assimilating blood velocity measures in hemodynamics simulations: preliminary results. *Proc. Comput. Sci.* **1** (1), 1231–1239.
- D'ELIA, M. & VENEZIANI, A. 2010*b* A data assimilation technique for including noisy measurements of the velocity field into Navier–Stokes simulations. In *Proc. of V European Conference on Computational Fluid Dynamics* (ed. J. C. F. Pereira & A. Sequeira), ECCOMAS CFD.
- DENARO, F. M. 2003 On the application of the Helmholtz–Hodge decomposition in projection methods for incompressible flows with general boundary conditions. *Intl J. Numer. Meth. Fluids* **3**, 43–69.
- FORMAGGIA, L., VENEZIANI, A. & VERGARA, C. 2008 A new approach to numerical solution of defective boundary value problems in incompressible fluid dynamics. *SIAM J. Numer. Anal.* **46** (6), 2769–2794.
- FORMAGGIA, L., VENEZIANI, A. & VERGARA, C. 2010 Flow rate boundary problems for an incompressible fluid in deformable domains: formulations and solution methods. *Comput. Meth. Appl. Mech. Engng* **199** (9–12), 677–688.
- FURSIKOV, A. V., GUNZBURGER, M. D. & HOU, L. S. 1998 Boundary value problems and optimal boundary control for the Navier–Stokes system: the two-dimensional case. *SIAM J. Control Optim.* **36** (3), 852–894.
- GARCIA, D. 2011 A fast all-in-one method for automated post-processing of PIV data. *Exp. Fluids* **50** (5), 1247–1259.
- GESSNER, F. B. 1973 Brief reviews: hemodynamic theories of atherogenesis. *Circ. Res.* **33** (3), 259–266.
- GUDBJARTSSON, H. & PATZ, S. 1995 The Rician distribution of noisy MRI data. *Magn. Reson. Med.* **34** (6), 910–914.
- GUERRA, T., SEQUEIRA, A. & TIAGO, J. 2015 Existence of optimal boundary control for the Navier–Stokes equations with mixed boundary conditions. *Port. Math.* **72**, 267–283.
- GUERRA, T., TIAGO, J. & SEQUEIRA, A. 2014 Optimal control in blood flow simulations. *Intl J. Non-Linear Mech.* **64**, 57–69.
- GUNZBURGER, M. D. & MANSERVISI, S. 2000 The velocity tracking problem for Navier–Stokes flows with boundary control. *SIAM J. Control Optim.* **39** (2), 594–634.
- HARDMAN, D., SEMPLE, S. I., RICHARDS, J. M. & HOSKINS, P. R. 2013 Comparison of patient-specific inlet boundary conditions in the numerical modelling of blood flow in abdominal aortic aneurysm disease. *Intl J. Numer. Meth. Biomed. Engng* **29** (2), 165–178.
- HAROUNA, S. K. & PERRIER, V. 2012 Helmholtz–Hodge decomposition on $[0, 1]^d$ by divergence-free and curl-free wavelets. In *Curves and Surfaces: 7th International Conference, Avignon, France, June 24–30, 2010, Revised Selected Papers* (ed. J. D. Boissonnat, P. Chenin, A. Cohen, C. Gout, T. Lyche, M. L. Mazure & L. Schumaker), pp. 311–329. Springer.
- HOCHAREON, P., MANNING, K. B., FONTAINE, A. A., TARBELL, J. M. & DEUTSCH, S. 2004 Wall shear-rate estimation within the 50cc Penn State artificial heart using particle image velocimetry. *Trans. ASME J. Biomech. Engng* **126** (4), 430–437.
- IDE, K., COURTIER, P., GHIL, M. & LORENC, A. C. 1997 Unified notation for data assimilation: operational, sequential and variational. *J. Met. Soc. Japan* **75** (1B), 181–189.
- JOHNSON, H. J., MCCORMICK, M., IBÁÑEZ, L. & CONSORTIUM, THE INSIGHT SOFTWARE 2013 *The ITK Software Guide*, 3rd edn. Kitware Inc.
- KATRITSIS, D., KAIKITSIS, L., CHANIOTIS, A., PANTOS, J., EFSTATHOPOULOS, E. P. & MARMARELIS, V. 2007 Wall shear stress: theoretical considerations and methods of measurement. *Prog. Cardiovascu. Dis.* **49** (5), 307–329.
- KOLIPAKA, A., ILLAPANI, V. S. P., KALRA, P., GARCIA, J., MO, X., MARKL, M. & WHITE, R. D. 2016 Quantification and comparison of 4D-flow MRI-derived wall shear stress and MRE-derived wall stiffness of the abdominal aorta. *J. Magn. Reson. Imag.* **45** (3), 771–778.
- KU, D. N., GIDDENS, D. P., ZARINS, C. K. & GLAGOV, S. 1985 Pulsatile flow and atherosclerosis in the human carotid bifurcation. Positive correlation between plaque location and low oscillating shear stress. *Arteriosclerosis* **5** (3), 293–302.

- LARSSON, D., SPUHLER, J. H., PETERSSON, S., NORDENFUR, T., COLARIETI-TOSTI, M., HOFFMAN, J., WINTER, R. & LARSSON, M. 2017 Patient-specific left ventricular flow simulations from transthoracic echocardiography: robustness evaluation and validation against ultrasound Doppler and magnetic resonance imaging. *IEEE Trans. Med. Imag.* **36** (11), 2261–2275.
- LEE, H. 2011 Optimal control for quasi-Newtonian flows with defective boundary conditions. *Comput. Meth. Appl. Mech. Engng* **200** (33–36), 2498–2506.
- MALEK, A. M., ALPER, S. L. & IZUMO, S. 1999 Hemodynamic shear stress and its role in atherosclerosis. *Am. Med. Assoc.* **282** (21), 2035–2042.
- MARKL, M., FRYDRYCHOWICZ, A., KOZERKE, S., HOPE, M. & WIEBEN, O. 2012 4D flow MRI. *Magn. Reson. Imag.* **36** (5), 1015–1036.
- MORBIDUCCI, U., PONZINI, R., GALLO, D., BIGNARDI, C. & RIZZO, G. 2013 Inflow boundary conditions for image-based computational hemodynamics: impact of idealized versus measured velocity profiles in the human aorta. *J. Biomech.* **46** (1), 102–109.
- PATANKAR, S. V. & SPALDING, D. B. 1972 A calculation procedure for heat, mass and momentum transfer in three-dimensional parabolic flows. *J. Heat Mass Transfer* **15**, 1787–1806.
- PELC, N. J., HERFKENS, R. J., SHIMAKAWA, A. & ENZMANN, D. R. 1991 Phase contrast cine magnetic resonance imaging. *Magn. Reson. Q.* **7** (4), 229–254.
- PIROLA, S., CHENG, Z., JARRAL, O. A., O'REGAN, D. P., PEPPER, J. R., ATHANASIOU, T. & XU, X. Y. 2017 On the choice of outlet boundary conditions for patient-specific analysis of aortic flow using computational fluid dynamics. *J. Biomech.* **60**, 15–21.
- RAFFEL, M., WILLERT, C. E., WERELEY, S. T. & KOMPENHANS, J. 2007 Post-processing of PIV data. In *Particle Image Velocimetry: A Practical Guide*, pp. 177–208. Springer.
- RENEMAN, R. S., ARTS, T. & HOEKS, A. P. G. 2006 Wall shear stress – an important determinant of endothelial cell function and structure – in the arterial system *in vivo*. Discrepancies with theory. *J. Vascul. Res.* **43** (3), 251–269.
- SCHMITTER, S., SCHNELL, S., UĞURBIL, K., MARKL, M. & DE MOORTELE, P. F. VAN 2016 Towards high-resolution 4D flow MRI in the human aorta using kt-grappa and b1+ shimming at 7 tesla. *J. Magn. Reson. Imag.* **44** (2), 486–499.
- SHAABAN, A. M. & DUERINCKX, A. J. 2000 Wall shear stress and early atherosclerosis: a review. *Am. J. Roentgenol.* **174** (6), 1657–1665.
- TEXON, M., IMPARATO, A. M. & HELPERN, M. 1965 The role of vascular dynamics in the development of atherosclerosis. *Am. Med. Assoc.* **194** (11), 1226–1230.
- THANG, C., BLATTER, D. D. & PARKER, D. L. 1995 Correction of partial-volume effects in phase-contrast flow measurements. *J. Magn. Reson. Imag.* **5** (2), 175–180.
- TIAGO, J., GUERRA, T. & SEQUEIRA, A. 2016 A velocity tracking approach for the data assimilation problem in blood flow simulations. *Intl J. Numer. Meth. Biomed. Engng.* **30** (10).
- DE VECCHI, A., GOMEZ, A., PUSHPARAJAH, K., SCHAEFFTER, T., SIMPSON, J. M., RAZAVI, R., PENNEY, G. P., SMITH, N. P. & NORDSLETTEN, D. A. 2016 A novel methodology for personalized simulations of ventricular hemodynamics from noninvasive imaging data. *Comput. Med. Imaging Graph.* **51**, 20–31.
- VORP, D. A. & GEEST, J. P. VANDE 2005 Biomechanical determinants of abdominal aortic aneurysm rupture. *Arterioscler. Thromb. Vascul. Biol.* **25** (8), 1558–1566.
- VORP, D. A., RAGHAVAN, M. L., MULUK, S. C., MAKAROUN, M. S., STEED, D. L., SHAPIRO, R. & WEBSTER, M. W. 1996 Wall strength and stiffness of aneurysmal and nonaneurysmal abdominal aorta. *Ann. N.Y. Acad. Sci.* **800**, 274–276.
- WALPOLA, P. L., GOTLIEB, A. I. & LANGILLE, B. L. 1993 Monocyte adhesion and changes in endothelial cell number, morphology, and f-actin distribution elicited by low shear stress *in vivo*. *Am. J. Pathol.* **142** (5), 1392–1400.
- WELLER, H. G., TABOR, G., JASAK, H. & FUREBY, C. 1998 A tensorial approach to computational continuum mechanics using object-oriented techniques. *Comput. Phys.* **12** (6), 620–631.
- WESTERWEEL, J. & SCARANO, F. 2005 Universal outlier detection for PIV data. *Exp. Fluids* **39** (6), 1096–1100.

- YOSHIDA, Y., SUE, W., OKANO, M., OYAMA, T., YAMANE, T. & MITSUMATA, M. 1990 The effects of augmented hemodynamic forces on the progression and topography of atherosclerotic plaques. *Ann. N.Y. Acad. Sci.* **598**, 256–273.
- ZAND, T., MAJNO, G., NUNNARI, J. J., HOFFMAN, A. H., SAVILONIS, B. J., MACWILLIAMS, B. & JORIS, I. 1991 Lipid deposition and intimal stress and strain. A study in rats with aortic stenosis. *Am. J. Pathol.* **139** (1), 101–113.
- ZARINS, C. K., ZATINA, M. A., GIDDENS, D. P., KU, D. N. & GLAGOV, S. 1987 Shear stress regulation of artery lumen diameter in experimental atherogenesis. *J. Vascul. Surg.* **5** (3), 413–420.